

THESIS

HYDROXYAPATITE STRUCTURES CREATED BY ADDITIVE MANUFACTURING
WITH EXTRUDED PHOTOPOLYMER

Submitted by

Katherine Vanesa López Ambrosio

School of Advanced Materials Discovery

In partial fulfillment of the requirements

For the degree of Master of Science

Colorado State University

Fort Collins, Colorado

Summer 2019

Master's Committee:

Advisor: Susan P. James

Kaka Ma

David A. Prawel

Copyright by Katherine V. Lopez Ambrosio 2019

All Rights Reserved

ABSTRACT

HYDROXYAPATITE STRUCTURES CREATED BY ADDITIVE MANUFACTURING WITH EXTRUDED PHOTOPOLYMER

Bone tissue has the ability to regenerate and heal itself after fracture trauma. However, this ability can be affected by different risk factors that are related to the patient and the nature of the fracture. Some of the factors are age, gender, diet, health, and habits. Critical-sized defects are particularly difficult, if not impossible, to heal correctly. Particularly in large defects, bone regeneration ability is impeded, disrupting normal healing processes, resulting in defective healing, integration, and non-union. To prevent and treat defective healing or non-union, surgical intervention is needed. Surgeons implant various forms of devices between the ends of the broken bone, usually with external fixation. Implants function by guiding and enabling new bone ingrowth while giving support to the healing tissue. Some of the most common implants are autografts, allografts, and metallic endoprostheses. Unfortunately, these common techniques have drawbacks such as the risk of infection and relatively poor biological or mechanical compatibility with host tissue, in addition to the limited source of donor tissue and high cost, often resulting from secondary surgical interventions. Critical defects are particularly problematic. Hence, there is a necessity for bone implant substitutes that diminish the risk of infection and incompatibility while also providing similar mechanical properties to real bone tissue. Hydroxyapatite (HAp) is a ceramic with a chemical composition similar to bone tissue that has shown biocompatibility and osteoconductive properties with host bone tissue, but it is difficult to manufacture into complex structures with mechanical properties comparable to bone tissue. Therefore, significant efforts are directed to produce materials and methods that could produce HAp synthetic implants to treat bone defects.

This research aimed to create and characterize a hydroxyapatite photo-polymeric resin suitable for 3D printing, which could produce dense HAp ceramic parts in complex shapes without requiring support material. We created a HAp-based photopolymer slurry that achieved 41 vol% HAp loading in homogenous slurries. The HAp slurries presented a strong shear thinning behavior and dispersion stability over 20 days under dark storage conditions. The resultant rheological behavior of HAp slurries enabled 3D printing of HAp green bodies in complex shapes using a combination of viscous extrusion and layer-wise photo-curing processes. Complex structures with concave and convex forms and scaffolds with interconnected pores ranging from 130 μm to 600 μm pore sizes and 10% to 40% porosity were successfully built with high resolution and no support material. Moreover, HAp/PEGDMA green bodies presented complete layer cohesion. After 3D printing, sintering was used to densify HAp structures and eliminate the polymer matrix. The resultant HAp structures maintained their complex details, had a relative density of $\sim 78\%$ compared to fully dense HAp and a dimensional shrinkage of $\sim 15\%$ compared to its green body. Sintered HAp structures were found to be non-cytotoxic for ADSCs cells. Flexural properties of HAp green and sintered structures were also determined. It was found that green bodies had a flexural strength of $\sim 30.42\text{MPa}$ comparable to trabecular bone.

To summarize, a photopolymerizable resin with 41 vol% of HAp was created to produce $\sim 78\%$ dense HAp complex structures. This was achieved by using additive manufacturing that combined viscous extrusion and layer-wise photo-curing and a sintering process. HAp/PEGDMA showed flexural strength comparable to the trabecular bone, and HAp sintered structures demonstrated non-cytotoxic behavior.

ACKNOWLEDGMENTS

I would like to thank my advisors Dr. David Prawel and Dr. Susan James for all the advice, guidance, patience, and time given during the past two years that helped me in this research. I am especially grateful with Dr. Prawel for trusting on my potential to develop research even when I did not know about additive manufacturing or biomaterials. He showed me for the first time a 3D printer and guided me in all this journey.

I am also grateful with Dr. James for being a mentor not just in academia but in my personal life. She believed in me and help me to realize my full potential as a woman in STEM fields. I also would like to thank my committee member Dr. Kaka Ma for all the guidance in this work and the permission to use different tools that were vital to the development of this research.

I would like to thank Colorado State University for providing the resources that made possible this research and all the personnel from the Central Instrumentation Facility for the guidance in the use of different instrumentation. Especially, I would like to thank Dr. Karolien Deneff, Dr. Patrick McCurdy, Dr. Roy Geiss, and Dr. Brian Newell.

Several other persons and laboratory groups deserve acknowledgment due to the contribution and collaboration in this work. Dr. Bailey and Dr. Popat for the use of their equipment in regular basis, Trevor Aguirre for his aid in the mechanical testing, Gabriel Wham for his efforts involved in the 3D printing process, Dr. Hieu Bui for the cytotoxicity studies, the Biomaterials Research and Engineering Laboratory (BREL) and Idea to Product laboratory (I2P) for the advice in many topics.

Additionally, I would like to thank my department School of Advanced Materials Discovery (SAMD) and my classmates that enriched this journey with knowledge, laughs, and good moments.

Finally, I am very grateful to my family for all the support, love, and encouragement during this time, pursuing my master's degree. My mom because even though she is not here anymore, she always encouraged me to dream big and work hard; my dad because he sold his dream to help me pay mine; my sister because she was always there when I needed someone; my fiancé because he brought so much happiness, support, and company into my life along this journey. *Los amo mucho.*

TABLE OF CONTENTS

ABSTRACT.....	ii
ACKNOWLEDGMENTS	iii
1. MOTIVATION AND SCOPE.....	1
1.1 Motivation.....	1
1.2 Scope.....	2
1.2.1 Project	2
1.2.2 Hypotheses.....	2
1.2.3 Specific Aims.....	2
2. INTRODUCTION	3
2.1. Bone.....	3
2.2. Hydroxyapatite (HAp)	7
2.3 Photopolymerization	8
2.4 Ceramics in colloidal systems.....	12
2.5 Additive manufacturing	15
2.6 Sintering of ceramics	19
3. MATERIALS AND METHODS.....	22
3.1. Materials	22
3.1.1. Monomer: Ethylene Glycol Dimethacrylate (EGDMA).....	22

3.1.2. Dispersant: Solplus D540.....	23
3.1.3 Photoinitiator: Diphenyl (2,4,6 trimethyl benzoyl) phosphine oxide.....	23
3.1.4. Ceramics: Hydroxyapatite.....	24
3.2. Methods of HAp pretreatment	26
3.2.1. Method to increase the particle size of Macron HAp.....	26
3.2.2. Method to decrease particle size of Mk Nano HAp.....	27
3.3. Resin formulation of 41vol% (67wt%) hydroxyapatite	28
3.4. Production of complex HAp structures: (3D printing)	29
3.5. Sintering of HAp complex structures.....	31
3.6. Flexural strength	34
3.7. Cytotoxicity studies	35
3.8. Statistics	36
4. RESULTS AND DISCUSSION	37
4.1. Pretreatment of HAp	37
4.1.1. Increasing particle size of Macron HAp	37
4.1.2. Decreasing particle size of MK Nano HAp	38
4.2. Resin formulation.....	40
4.2.1. HAp resin viscosity and homogeneity	42
4.3. Production of complex HAp structures.....	46
4.4. Sintering of HAp complex structures.....	50

4.5. Flexural Strength.....	56
4.6. Cytotoxicity Studies in sintered HAp samples.....	63
5. CONCLUSIONS.....	64
6. SUMMARY OF WORK AND FUTURE DIRECTIONS.....	66
REFERENCES	69
APPENDIX 1: 41% Vol hydroxyapatite slurry mixing protocol.....	73
APPENDIX 2: Rheology measurements procedure	75
APPENDIX 3. Protocol to polish HAp/PEGDMA samples	78
APPENDIX 4: Power density of 405nm light source Hyrel 3D printer	81

LIST OF TABLES

Table 1. Mechanical properties of human bone. Adapted from [11].....	5
Table 2. Hydroxyapatite characteristics.....	25
Table 3. Sample treatment to increase particle size.....	26
Table 4. Conditions of experiments to decrease particle size.....	28
Table 5. DOE sintering varying T2 and R2.....	32
Table 6. Sintering DOE.....	51
Table 7. Flexural properties of green and sintered bodies.....	59
Table 8. Mechanical properties of scaffolds created by other authors	59

LIST OF FIGURES

Figure 2.1. Hierarchical morphology of bone	4
Figure 2.2 Healing process of bone after fracture trauma.	6
Figure 2.3. HAp unit cell. Red spheres represent hydroxyl groups.	7
Figure 2.4. Radical polymerization mechanism.	10
Figure 2.5. Cure depth profile of photopolymerization	11
Figure 2.6. Electrostatic, steric and electrosteric dispersion	13
Figure 2.7. Types of rheological behavior of colloidal systems.	15
Figure 2.8. 3D printing technologies used in tissue engineering	17
Figure 2.9. Evolution of dihedral angle in the sintering process	20
Figure 2.10. Stages of sintering	21
Figure 3.1 Ethylene glycol dimethacrylate molecule	22
Figure 12. Photoinitiator molecule diphenyl (2,4,6, trimethyl benzoyl) phosphine oxide	23
Figure 3.2. absorption spectra of TPO	24
Figure 3.3. SEM images of as received HAp initial morphology.	26
Figure 3.4. Schematic of the 3D printing process.	30
Figure 3.5. Sintering profile used to densify HAp structures. R	31
Figure 3.6. SEM image of HAp densified surface	34
Figure 3.7. 4-point bending tester	35
Figure 4.1. As received Macron HAp particles.	38
Figure 4.2 As received MK Nano HAp particles	39
Figure 4.3. Particle size MK Nano HAp after ball milling t	40

Figure 4.4. Dried HAp resin in milling jar with black agate milling balls.	42
Figure 4.5. Shear thinning rheological behavior of HAp slurries.	43
Figure 4.6. viscosity of HAp slurries during the first 20 days after synthesis.	44
Figure 4.7. SEM image of HAp/PEGDMA green body surface.	45
Figure 4.8. SEM image of HAp/PEGDMA green body surface.	46
Figure 4.9. 3D printed complex structure	47
Figure 4.10. HAp/PEGDMA scaffolds	48
Figure 4.11. Layer cohesion of HAp samples.	49
Figure 4.12. X-ray diffraction pattern of HAp sintered structures.	50
Figure 4.13. SEM images of surface densification of HAp samples r	52
Figure 4.14. Average grain size and Relative density	54
Figure 4.15 Different densification presented in HAp sintered structures.	55
Figure 4.16. Shrinkage of HAp samples.	56
Figure 4.17. Characteristic flexural Stress vs. Strain curves	57
Figure 4.18. Flexural Modulus and flexural strength	58
Figure 4.19. Fracture surface of green bodies.	60
Figure 4.20. Fracture surface sintered HAp.	61
Figure 4.21. Schematic explaining cause for different densification.	62
Figure 4.22. LDH Activity of sintered HAp samples for day 7,14 and 28.	63
Figure 6.1. Sintered scaffold with residual and design porosity	68

1. MOTIVATION AND SCOPE

1.1 Motivation

Bone tissue has the ability to regenerate and heal itself after fracture trauma. However, this ability can be affected by different risk factors that are related to the patient and the nature of the fracture. Some of the factors are age, gender, diet, health, and habits [1]. If the bone regeneration ability is affected, the healing of the bone tissue is disrupted, producing defective healing or non-union.

To prevent and treat defective healing or non-union, surgical intervention is needed. Surgeons implant an external fixator between the ends of the broken bone. The implants function by guiding the ingrowing new bone and giving support to the rest of the bone while the fracture is healing. Some of the most common implants are autografts, allografts, and metallic endoprostheses. Autografts are implants that come from the tissue of the same patients and are considered the gold standard [2]; allografts are tissue implants that come from other patients and metallic endoprosthesis are metallic structures attached to the bone. Unfortunately, these common techniques have drawbacks such as major risk of infection and incompatibility¹, in addition to the limited source of donor tissue and high cost, often resulting from common secondary surgical interventions [4,5].

Hence, there is a necessity for bone implant substitutes that diminish the risk of infection and incompatibility while also providing similar mechanical properties to real bone tissue in a cost-effective manner. In particular to manufacture custom bone implants with chemical,

¹ Compatibility: Acceptance of an external implant by the body and surrounding tissues without irritation, abnormal inflammatory response and/or immunological reactions while matching the mechanical, optical and design properties [3].

morphological, and mechanical similarity with the host bone tissue. Therefore, this project focused on developing a HAp slurry that could be 3D printed into complex shapes and custom bone surrogates.

1.2 Scope

1.2.1 Project

Create and characterize a hydroxyapatite photo-polymeric resin suitable for 3D printing that can produce dense ceramic parts with complex geometries.

1.2.2 Hypotheses

1. A photopolymer loaded with a high content of hydroxyapatite (HAp) can be created with appropriate rheological behavior to 3D print complex objects without support material.
2. High-density hydroxyapatite structures can be created with a high-load hydroxyapatite photopolymer resin that can be 3D printed and sintered.

1.2.3 Specific Aims

1. Create a photo-polymeric slurry with a high content of HAp with a suitable balance between viscosity and solid load to be 3D printed
2. 3D print complex structures.
3. Test mechanical strength of printed and sintered structures.

2. INTRODUCTION

2.1. Bone

Bone is a vital organ in vertebrate animals. Its structure and composition have the function of mechanical integrity for locomotion and protection, and participation in mineral homeostasis metabolic pathways. It is a composite of organic and inorganic materials. By volume, the composition of bone tissue corresponds to 40% of inorganic matter, 25% water, and 35% organic matter. [6,7]

From the inorganic components of human bone, 95w% corresponds to an impure calcium phosphate phase known as hydroxyapatite $\text{Ca}_{10}(\text{PO}_4)_6(\text{OH})_2$. Its crystals are 20-80nm in length, 2-5nm in thickness, and 15nm in width [6]. The other 5% is constituted by common impurities in HAp crystals such as carbonate, magnesium, potassium, strontium, sodium, chloride, and fluoride. These impurities replace apatite sites or hydroxyl groups in the crystalline structure, reducing crystallinity and producing changes in biological and/or mechanical properties of the bone, for example, increasing mechanical strength [8,9].

From the organic components, 98w% is collagen type I. This is a protein with low solubility that plays a major role in the structure of the bone matrix. Its chemical morphology is a very rigid linear chain organized in triple helix structure, 300nm in length. Other components of the organic phase represent just 2w%, and their biological contributions are mainly in the remodeling of bone. These regulate and affect precursors to bone growth, such as mineral maturation, mineral binding, cell-binding, and bone cell differentiation [9].

Bone has a hierarchical organization where extremely well-organized structures are inherent at any scale as can be seen in figure 2.1. At a macro scale, bone is composed of trabecular and cortical bone. Trabecular bone has a sponge structure with 40% porosity where HAp is ordered in platelets

and rods in the vertical direction between the pores. Cortical bone is 20% porosity and has four times the mass of the trabecular bone. At a mesoscale, bone is organized by osteons surrounding Haversian canals (neurovascular canals). At a microscale, osteons are ordered in a lamellar form. The lamella is composed of collagen fibrils in a hierarchical structure constituted of HAp crystals, and collagen helix arrange.

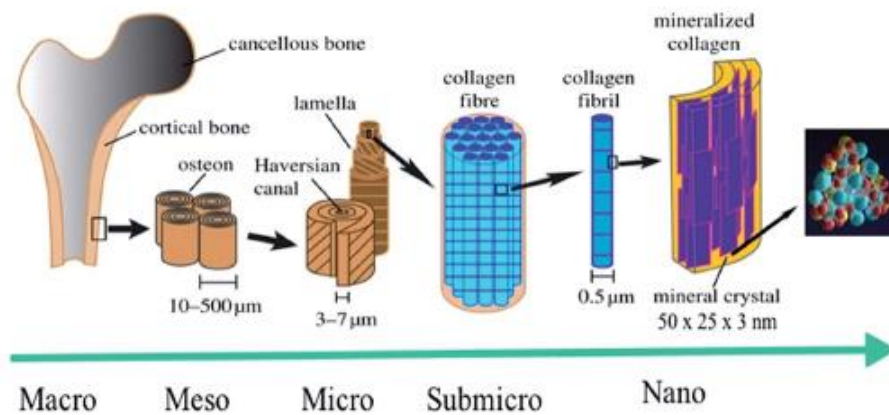


Figure 2.1. Hierarchical morphology of bone [9]

The mechanical strength of the bone depends on this hierarchical structure, especially the tight packing of the osteons [7]. Inorganic components are responsible for the compression strength and stiffness, organic components for tensile properties, and all the components organized in a hierarchy that provides high toughness [10]. Mechanical properties of human bone are summarized in table 1.

Table 1. Mechanical properties of human bone. Adapted from [11]

Human	Tensile strength (MPa)	Compressive strength (MPa)	Flexural strength (MPa)	Elastic modulus (GPa)	Porosity (%)
Cortical Bone	50-151	100-150	135-193	10-20	5-10
Trabecular bone	1-5	2-12	10-20	0.1-5	50-90

A bone fracture is caused by excessive stress, greater than the bone strength or fatigue failure produced by cyclic activity loads that accumulate damage. An auto-activated healing restorative process begins to return the tissue to its original structure, returning its functionality. However, not all fractures heal completely or recreate the original properties of the tissue. Often, depending on the patient's health and the surrounding environment of the fracture, non-union, or defective unions occurs [7,10]. Giannoudis et al. have stated four important factors, known as the diamond concept, that contribute to bone restoration: Osteogenic cells, osteoconductive scaffolds, mechanical environment, and growth factors [12].

Typically, a normal bone healing process is divided into three overlapping stages: the early inflammatory stage, the repair stage, and the late remodeling stage. This is shown in figure 2.2. After the bone fractures, the early inflammatory stage that lasts four days begins by filling the fracture gap space with blood from the ruptured vessels and creating a hematoma. Then, macrophages² remove the debris from the fracture, initial granulation tissue is generated, and osteoblast and mesenchymal cell migrate to the fracture sites. In the repair stage that lasts about 4 to 6 weeks, mesenchymal cells differentiate into fibroblasts, chondrocytes, or osteoblasts. Fibroblasts construct stroma to support vascular ingrowth and osteoblasts secret minerals to form

² Macrophages: Blood cell of the immune system that digest cellular debris, microbes and foreign substances.

primary soft callus that ossifies to bridge the fracture sites. Finally, in the remodeling stage, which can take several months, fracture healing is completed with the aid of mechanical stress applied to the bone. The soft callus is remodeled to restore the original structure and shape [7,10,13].

Depending on the severity, degree of the extent, and the nature of the fracture, for successful healing fracture processes, the aid of an implant is necessary. Optimal bone implants should be osteoconductive, osteoinductive, osteogenic, biocompatible, bioresorbable, not prone to infection and fibrotic reaction, accessible, compatible with the mechanical strength of host bone tissue and cost-effective [2].

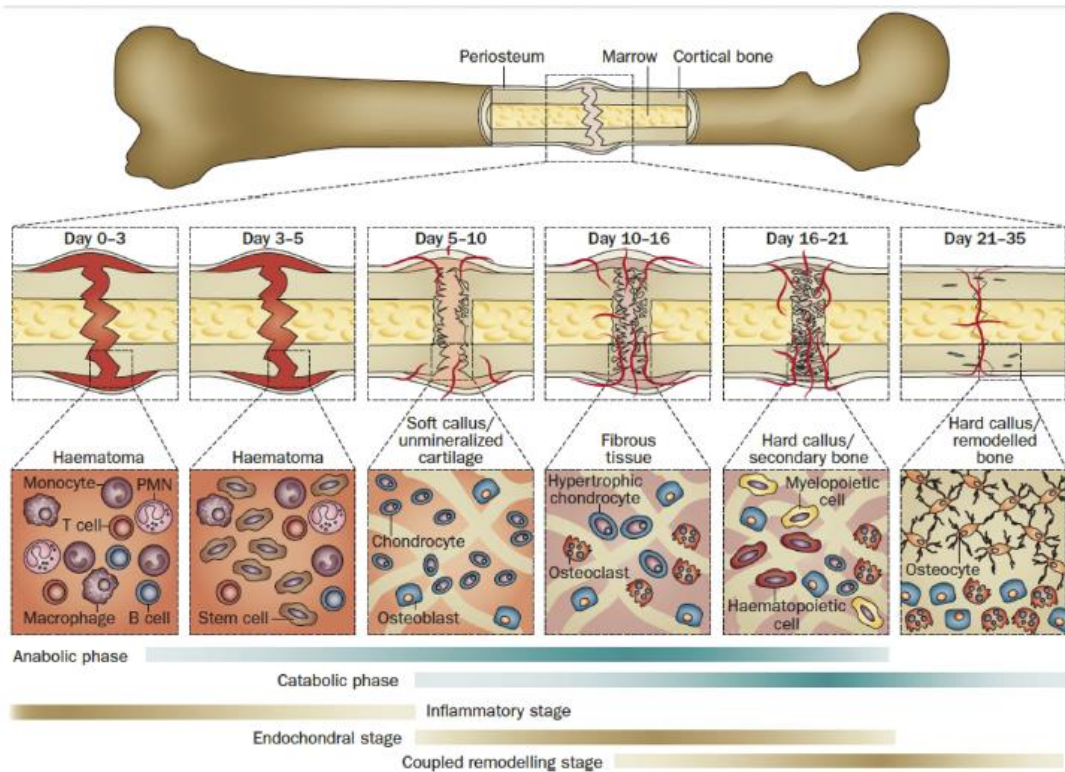


Fig. 2. Illustration of a typical fracture healing process, biological events, and cellular activities at different phases. The primary metabolic phases (blue bars) of fracture healing overlap with biological phases (brown bars). The time scale of healing is equivalent to a mouse closed femur fracture fixed with an intramedullary rod. Abbreviations: PMN, polymorphonuclear leukocyte. Reprinted by permission from Macmillan Publishers Ltd: Nature Reviews Rheumatology [34], copyright (2014).

Figure 2.2 Healing process of bone after fracture trauma. Day 0 to 5 represent the inflammatory stage, day 5 to 16 represent repair stage and day 16 to 35 represent remodeling stage [4]

2.2. Hydroxyapatite (HAp)

Hydroxyapatite is a calcium phosphate inorganic salt with a chemical composition in the unit cell of $\text{Ca}_{10}(\text{PO}_4)_6(\text{OH})_2$. The ceramic has a hexagonal $\text{P6}_3/\text{m}$ crystalline structure with an idealized Ca/P ratio of 1.67 as can be seen in figure 2.3.

Although the decomposition temperature, morphology, and chemical properties of HAp vary depending on the fabrication method [8,14], both synthetic and naturally-produced HAp have shown biocompatibility with host bone tissue [15–17].

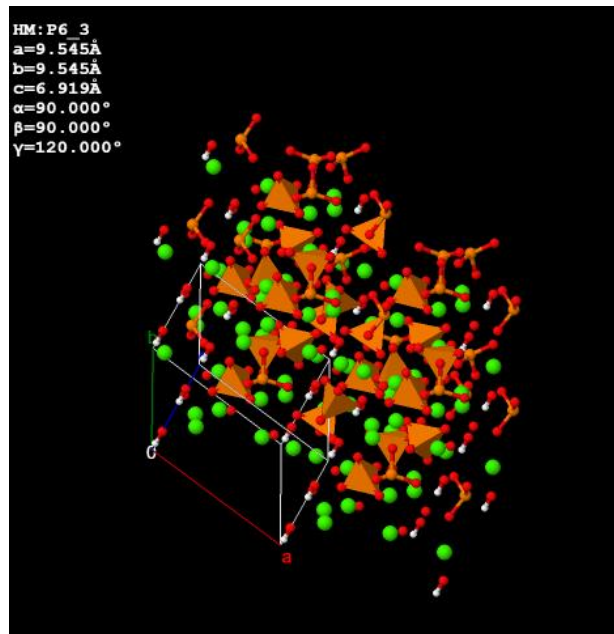


Figure 2.3. HAp unit cell. Red spheres represent hydroxyl groups. Green spheres represent calcium and orange triangles represent phosphate groups [19]

Chemical components of HAp correspond approximately to 60-70 wt% of human bone and 98 wt% of teeth [14]. HAp and other calcium phosphate phases such as alpha-tricalcium phosphate (α -TCP), beta-tricalcium phosphate (β -TCP) have been extensively investigated for biomedical applications due to the chemical similarity with bone tissue and osteoconductive³ properties [8].

³ Osteoconductive: ability of biomaterial to serve as a template or scaffold for bone cells and permit bone growth on its surface or down into porous structures. [8]

α -TCP, β -TCP, and HAp can transform into each other under different temperature and/or pressure conditions.

In comparison to TCPs and other calcium phosphate phases, HAp has greater mechanical strength due to the presence of a hydroxyl group, and the dissociation of Ca^{+2} and (PO_4^{-3}) ions at equilibrium in simulated body fluid studies is minimal. This dissociation decreases with increasing degree of stoichiometry in HAp [18]. In fact, due to the Ca and P ion's rapid dissolution and supersaturation of TCPs, it was determined through in-vitro studies that high degradation and dissolution of the Ca-P may compromise the mechanical strength of the biomaterial before new bone is formed. Additionally, high local concentrations of Ca-P ions can be harmful to the cells, as they trigger an acidic microenvironment that may demineralize the bone matrix. Thus, different ratios of HAp/TCP are being studied to optimize the degradation rate while proving mechanical strength [8].

2.3 Photopolymerization

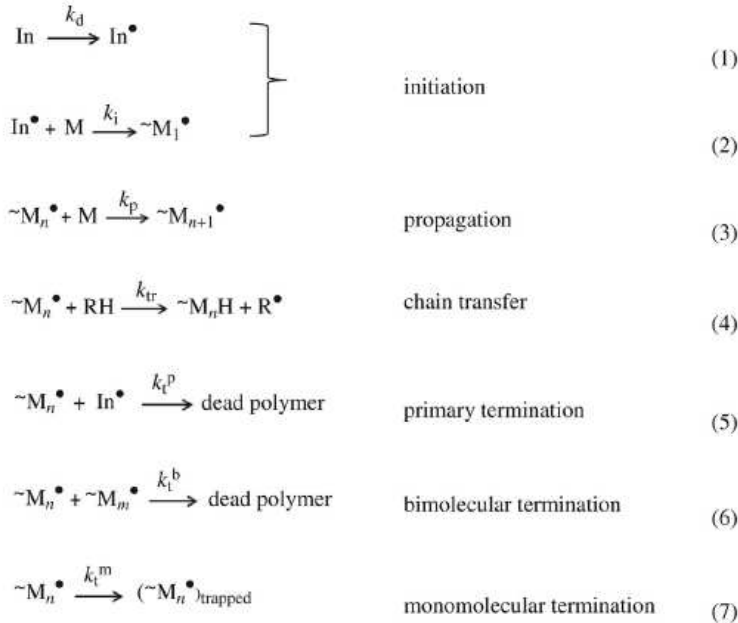
Photoinduced polymerization, also known as photopolymerization, is the synthesis of macromolecules by the reaction of monomers and/or oligomers with a reactive photoinitiator (PI). Common oligomers used in photopolymerization are acrylates and methacrylates due to the high reactivity of the carbon-carbon double bond in the presence of a free radical [19].

Photoinduced polymerization is advantageous compared to thermal induced polymerization as it is solvent free, has a fast reaction rate, and requires low energy to trigger polymerization. Moreover, photopolymerization is very flexible because it enables the production of highly crosslinked systems in a wide range of environmental and chemical conditions, such as the type

of monomer, wavelength, type of initiator, the power density of the light, temperature, among others [20].

When a photoinitiator produces a free radical by absorption of a photon, the polymerization reaction is known as free radical polymerization. PIs are classified by the mechanism in which they can produce free radicals upon irradiation. Type I corresponds to unimolecular systems where C-C bond undergo homolytic α -cleavage while type II are bimolecular systems that interact to extract hydrogen from one to another to split a bonding pair of electrons. [21]

Type I PI's are more commonly used in industry and academia due to their chemical simplicity, low transition energies, and high wavelength transition closer to the visible range. Regardless of the type of PI used in the free radical photopolymerization process, the reaction mechanism follows a process that includes initiation, propagation, chain transfer, and termination [19,20,22]. This is shown in figure 2.4.



SCHEME 2.1 Steps of the Free Radical Polymerization

In, M, and RH denote initiator, monomer, and chain transfer agent molecules, respectively; $\sim\text{M}_n^\bullet$ and M_n^\bullet are macroradicals k_d is initiator decomposition rate constant; k_i is initiation rate coefficient; k_p is propagation rate coefficient; k_{tr} is chain transfer rate coefficient; and k_t^p , k_t^b , and k_t^m are primary, bimolecular, and monomolecular termination rate coefficients, respectively.

Figure 2.4. Radical polymerization mechanism. [19].

Initiation is triggered by light irradiating on the PI, thus creating a free radical. Then, the PI free radical reacts with a monomer or oligomer, generating the first macroradical (a free radical in the monomer). Subsequently, propagation reactions occur where other monomers/oligomers react with macroradicals and propagate the molecular chains. Finally, depending on the experimental conditions, the reactions terminate through a variety of mechanisms, so the macromolecules stop growing. Primary terminations arise when the macromolecules react with primary radicals. This is common in systems where there is excessive PI concentration and/or light intensity. Bimolecular terminations occur when the macromolecules couple with other macromolecules. This mechanism is common in systems with inhibitors, which act as macromolecules. Monomolecular terminations occur when the photopolymer system becomes so viscous or rigid that the free radicals are trapped, and diffusion of the reactive centers is occluded.

Moreover, properties of the light source and system to be polymerized, such as penetration depth (D_p), irradiance, power density, and its interaction define different characteristics such as curing depth (C_d) and Line width (L_w) in the photopolymerizable system. Figure 2.5 shows the curing profile of a system (resin) that is being photopolymerized by a point laser beam of width (W_0).

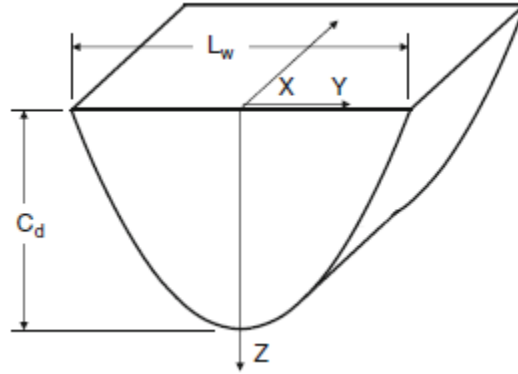


Figure 2.5. Cure depth profile of photopolymerization [23]

Curing depth (C_d) for Figure 2.5 profile is given by

$$C_d = D_p \left[\sqrt{\frac{2}{\pi} \frac{P_L}{W_0 V_S E_C}} \right] \quad (1)$$

Where P_L is the output power of laser (W), W_0 is the radius of the laser beam focused on the resin, V_S is the scan speed of the laser (mm/s) and E_c is the critical exposure (mJ/mm^2). For simple systems containing no dispersed solids, L_w is proportional to W_0 and function of C_d and D_p , and its relationship is described in the following equation (2).

$$L_w = W_0 \sqrt{\frac{2C_d}{D_p}} \quad (2)$$

For photopolymerization systems containing dispersed solids, depth of penetration, and curing depth depends on the energy of the light source, nature of the dispersed phase, and interactions between them. Light diffraction, scattering, refractive index and absorption of dispersed particles

play an important role in the curing depth of a photopolymerizable resin containing solids due to the effects of attenuation on the penetration depth [24].

2.4 Ceramics in colloidal systems

Colloids are systems formed by the dispersion of one material in another. Normally, the dispersed material is thermodynamically unstable with respect to the medium but can be stabilized kinetically, by minimizing the Gibbs free energy [25]. This stability depends on the surface potential of the particles, charge of the medium, and energy product of the interaction between particles, among other factors.

All colloids have four key parameters of the dispersed phase that determine their dispersion stability: particle size, volume fraction and physicochemical properties, and interparticle interactions. For concentrated systems, stability is produced by the formation of a network that only changes due to a consolidation process. Depending on the strength of this network and the properties of the dispersed phase, different rheological properties of the colloid are developed [26].

Interparticle interactions in a liquid result from repulsive and attractive energy forces. The more repulsive the forces between the particles, the more stable the colloid. Conversely, if the attractive forces are stronger than the repulsive forces, the particles agglomerate and produce clusters. Therefore, it can be stated that the stability of a colloidal system will depend on the energy interaction between particles.

The attractive forces, also known as Van der Waals interactions, are produced by the Keelson interactions (dipole-dipole), Debye interactions (dipole-induced dipole) and the London

dispersion. Van der Waals forces are a function of the distance between particles and temperature [25].

The repulsive forces between particles can be produced by electrostatic and/or steric interactions. These are shown in figure 2.6. Electrostatic forces are the result of charge developed by the adsorption of ions from the liquid onto the surface of the particles. These trigger a surface charge known as the diffuse double layer [27]. The repulsive energy due to electrostatic interactions depends on the strength and thickness of these layers.

Steric forces are produced by the interference of macromolecule layers adsorbed onto the surface of the particles, physically obstructing agglomeration. In the overlap region, the polymers interact, increasing the polymer density, and causing a different chemical potential. In general, the hydrodynamic radius created by the polymeric layers must be sufficiently thick and dense for repulsion energy to overcome the Van der Waals attraction energy [27]. This repulsion is represented in figure 2.6.b. Moreover, electrosteric repulsion is the product of the electrostatic and steric forces and is shown in figure 2.6.c.

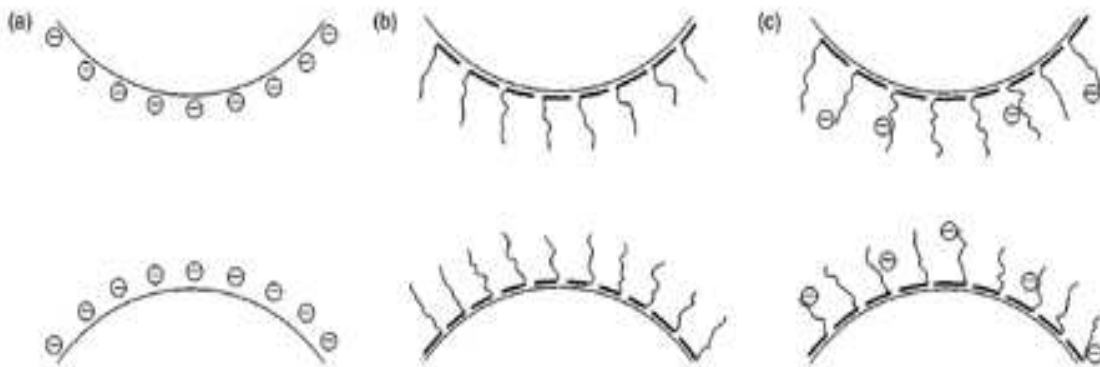


Figure 2.6. (a) Electrostatic, (b) steric and (c) electrosteric dispersion [26]

DVLO theory was developed to describe the stability behavior of colloidal systems that have Vander Waals and electrostatic interactions. According to this theory, the particles must overcome an energy barrier (G_{\max}) to defeat the diffuse double layer and form agglomerates. The larger the energy barrier, the lower the probability for the system to flocculate (e.g., form unwanted clumps). The repulsive energy decreases while the attractive energy increases with direct proportionality to the distance between particles. However, different researchers have modified this theory to include other types of interactions, such as steric forces [25].

Rheology in colloids is one of the most important properties because suspension, structure, and stability can be determined by flow behavior and vice versa. Different rheological behaviors exhibited by colloidal systems are shown in figure 2.7. Normally for colloids with low solids loading, a Newtonian behavior is observed, while for high solid loading, a shear thinning behavior is detected. Newtonian behavior is when the viscosity is independent of shear rate; shear thinning behavior is when the viscosity decreases with increasing of shear rate, and shear thickening is when viscosity increases with increasing shear rate.

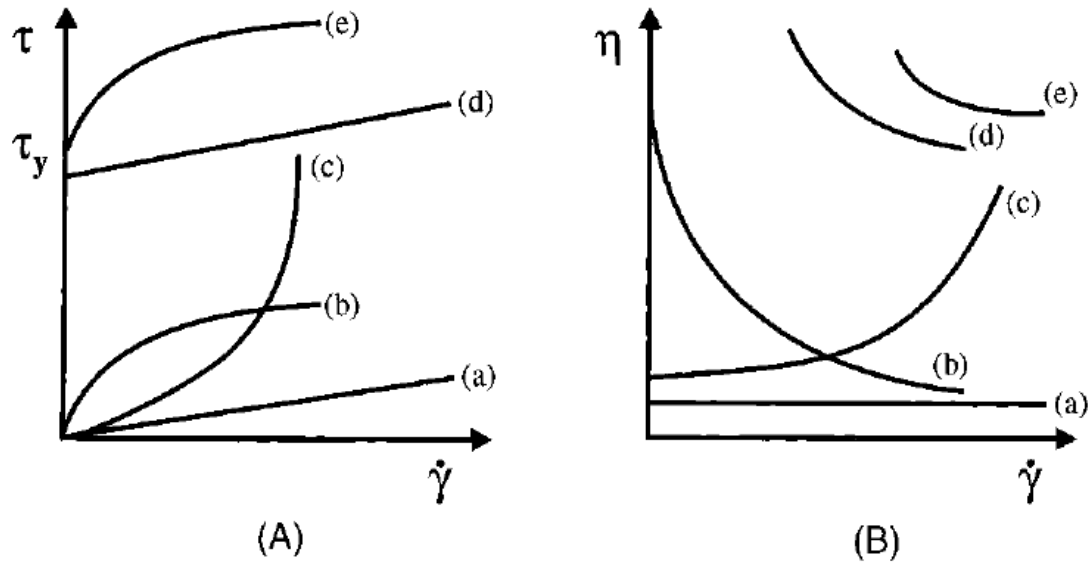


Figure 2.7. Types of rheological behavior of colloidal systems. (a) Newtonian flow; (b) shear thinning; (c) shear thickening; (d) Bingham plastic; and (e) pseudoplastic with yield stress [28]

2.5 Additive manufacturing

Additive manufacturing (AM), also known as 3D printing, is a process in which a 3-dimensional Computer-Aided Design (CAD) model is built by adding material in layers. These thin layers constitute the cross-sectional area of the computational design [23,29,30]. Different techniques of AM have been developed through the years using many different materials, essentially with the purpose of increasing the accuracy and properties of manufactured structures. Accuracy is highly depended on the layer thickness, AM technique, and material.

In orthopedic applications, numerous researchers have created different materials to 3D print implants for regeneration and tissue engineering of human bone. They have used common AM

techniques such as vat polymerization, powder bed fusion, material extrusion, binder jetting, or a combination of these methods. These are shown in figure 2.8.

In general, in AM of bone replacements, researchers have used bio-ceramics, biopolymers, bio-glasses, and biocompatible metals [29,31–34]. However, different challenges are presented when trying to achieve the needs stated in the diamond concept for successful fracture healing with the bone substitutes (see section 2.1). Some of the researchers have approached the mechanical strength of cortical or trabecular human bone (fatigue resistance, flexural strength, compressive strength), and others, the biological properties (regeneration, remodeling), but none have accomplished both. This is due to the limitations related to the material or/and AM technique. For instance, when using vat polymerization, the viscosity of the resin must be low enough that the resin essentially moves freely, which prevents the use of highly viscous resins. Highly viscous resins normally contain high ceramic loads, which increase the mechanical strength of the bone surrogates [28].

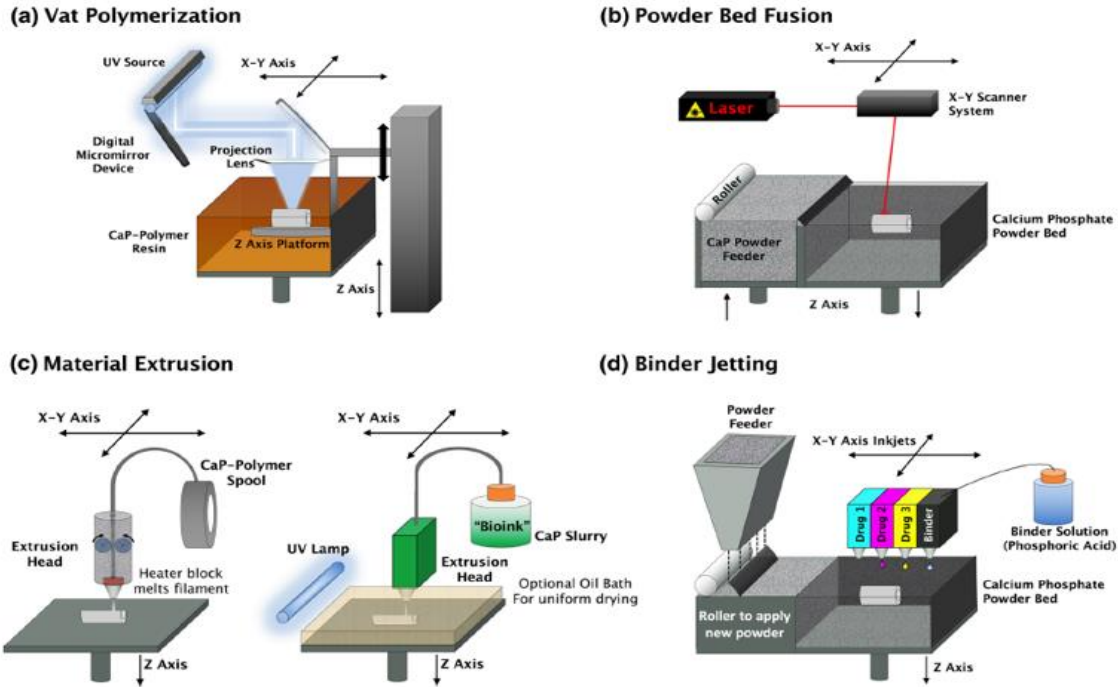


Figure 2.8. 3D printing technologies used in tissue engineering (a) vat polymerization, (b) powder bed fusion (c) material extrusion and (d) binder jetting [29]

Duan et al. produced nanocomposite scaffolds of calcium phosphate-poly (hydroxybutyrate-co-hydroxyvalerate (Ca-P/PHBV) and carbonate HAp-Poly (l-Lactic acid) using powder bed fusion. They seeded their scaffolds with human osteoblast-like cells. These scaffolds exhibited a compressive strength of 0.25MPa, well below human bone. Moreover, the cells had high cell viability, normal morphology, and successful cell proliferation after 21 days of incubation [35]. However, using powder bed fusion as a 3D printing process for orthopedic applications is limited by the cost of the process, restricted to one material, and requires high power [23].

Nandi and Bose et al. used binder jetting to produce TCP scaffold doped with SiO_2 and ZnO . In a rabbit tibia model, they studied the osteogenic, angiogenic, and compressive properties of the scaffolds. After doping and sintering, the scaffolds had a relative density of 94.1% and compressive strength 10.21MPa, higher than human trabecular bone but well below cortical bone.

Moreover, after four months the doped TCP scaffolds showed intense fibro-osteoid proliferations around the Haversian canals and enhanced osteoblastic activity and vascularization [36].

Gao et al. used binder jetting with UV light exposure to 3D print a bio-ink of suspended human-derived mesenchymal stem cells (hMSC) in PEGDMA-HAp-Bioactive Glass. Their synthetic tissues presented a cell interaction viability of 87% and a compressive modulus of 0.359MPa *in vitro* studies after 21 days [37].

Many researchers have created promising bone surrogates by viscous extrusion of calcium phosphate-based slurries. Jakus et al. created a biomaterial “ink” to 3D print hyperelastic bone scaffolds using material extrusion with solvent vaporization. The biomaterial was composed of 90wt% polycaprolactone or poly (lactic-co-glycolic acid), and 10wt% HAp. The materials presented a tensile modulus of 4.3 ± 0.4 MPa and 10.3 ± 1.3 MPa, respectively. After four weeks, the hyperelastic bones showed cell viability, proliferation, and osteogenic⁴ differentiation [38,39] though this material cannot be used to build bone surrogates for load-bearing applications due to its elastic nature.

Roohani-Esfahani et al. printed bioglass scaffolds by viscous extrusion with solvent vaporization. The scaffolds showed a mechanical strength comparable to the cortical bone with compressive strength of 110MPa and flexural strength of 30MPa. Moreover, they demonstrated *in vitro* and *in vivo* bioactivity. However, their scaffolds are not bioresorbable [31].

Koski et al. developed a slurry combining a natural polymer (starch) with 54 wt% HAp. The scaffolds were built by extrusion and showed a compressive strength of 10.35MPa. *In vitro* studies,

⁴ Osteogenic: Is the ability of the graft to produce new bone independently of the presence of live bone cells in the graft[7].

osteoblast cells showed favorable cell attachment and spreading, but these decreased the days after due to the dissolution of the scaffolds [40].

Many other researchers have tried to develop biocompatible, osteogenic, and resorbable implants. However, they have encounter drawbacks as their final parts do not have similar mechanical strength, cause fibrotic encapsulation in the patients' body, or does not match the biological needs for growing new bone. Moreover, while promising bone scaffolds have been produced, limited complexity in the structures has been achieved. Thus, new approaches have arisen that combine different AM techniques or materials to overcome the challenges mentioned above.

Asif et al. and Farahani et al. combined viscous extrusion with photopolymerization to produce self-supported and free forming structures. Both mixed fumed silica with photopolymers to achieve complex 3D printing designs with no support [41,42]. While their approach was not directed for bioengineering applications and are the first attempts to use viscous extrusion and photopolymerization, this combination of techniques could be used to print bone scaffolds with complex shapes that balance mechanical and biological properties choosing suitable materials.

2.6 Sintering of ceramics

Sintering is a method to consolidate particles by increasing temperature and sometimes pressure to enable atomic mobility. The atom mobility can be due to diffusion, vapor transport, plastic flow, viscous flow, mass flow, and dislocation climb. Metals and ceramics commonly undergo sintering processes to produce compact and dense materials, modify their morphology or/and mechanical properties.

The sintering global driving force is the surface elimination that triggers a decrease of grain boundaries, and total free energy in the system. This occurs by the diffusion of the atoms in the interface of the grains. The local driving force is given by the curvature potential that drives the local diffusion of atoms. When the total energy of a system of particles decreases a neck between them begins to grow and stops when an angle between them reaches the equilibrium angle (ϕ , dihedral angle) [43]. In figure 2.8, the evolution of the dihedral angle is shown as two non-spherical particles are sintered.

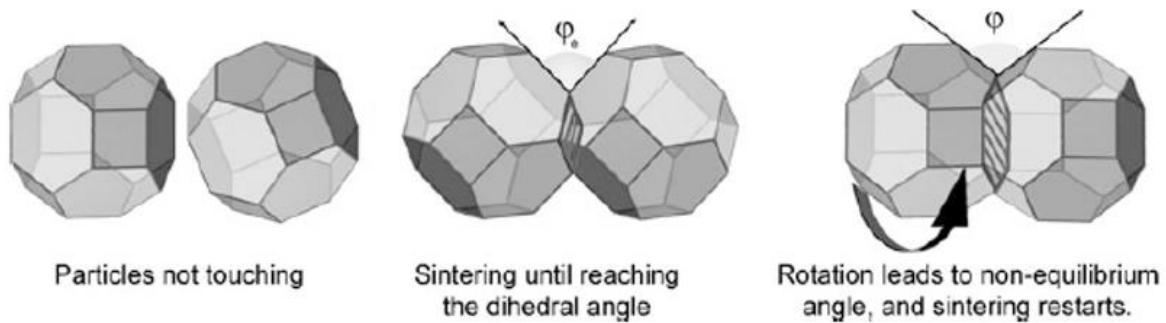


Figure 2.9. Evolution of dihedral angle in the sintering process [43]

Different processes can be observed in sintering depending on the system. Coalescence is one of them and represents the mechanism in which a small particle is dragged by a larger one because the higher curvature and surface elimination of the small particle works as the driving forces.

There are three stages in a sintering process. The first stage corresponds to the neck growth of the particles where a significant loss of surface area occurs. Then, in the second stage, most of the open porosity vanishes, grain size increases, and densification increase rapidly. Finally, in the third stage, densification is almost negligible, and grain size continues increasing. This is shown in figure 2.10.

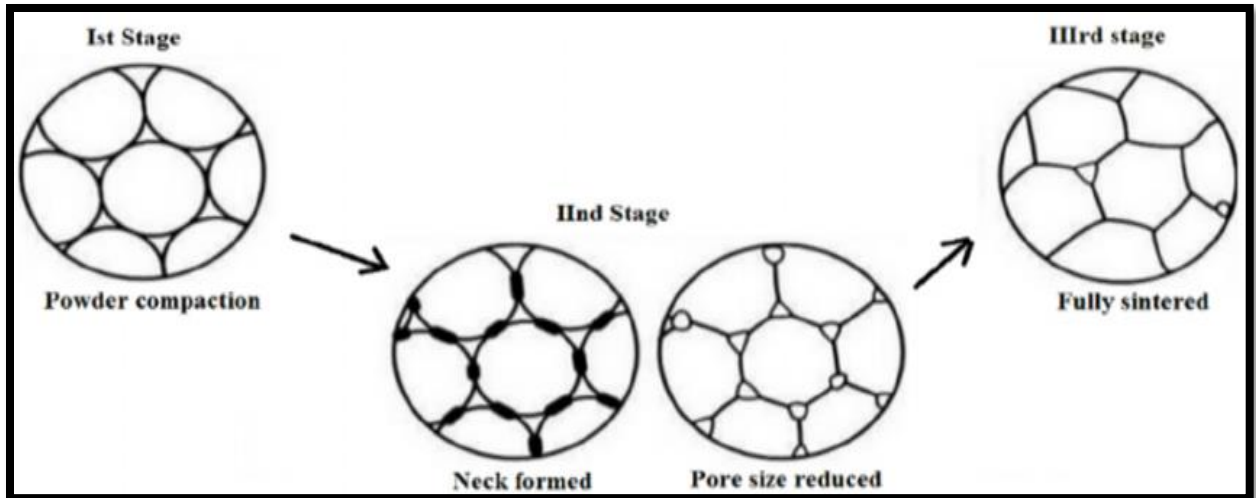


Figure 2.10. Stages of sintering [44].

Sintering bio-ceramics has become a common practice to densify the structures and enhance their mechanical strength. Although, microstructure after sintering is depended on powder properties, morphology, uniformity, agglomeration, degree of crystallinity, and surface area of the precursor particles [44].

3. MATERIALS AND METHODS

3.1. Materials

3.1.1. Monomer: Ethylene Glycol Dimethacrylate (EGDMA)

A light-sensitive liquid monomer was needed to suspend HAp particles and enable viscous extrusion and photopolymerization in the 3D printing process. In the colloidal stage, the liquid monomers assure flowability properties of HAp while in the 3D printed solid structure, the crosslinked network of monomers immobilize HAp particles in a specific shape and provide support. Prior work developed by another student found that HAp interactions with low viscosity solvents determined that that Ethylene glycol dimethacrylate (EGDMA) resulted in less aggregation of HAp compared to other solvents.

EGDMA with 99% purity and an inhibitor content of 110ppm of 3-methoxyphenol was purchased from Scientific Polymer Products, Inc. These multifunctional monomers have a molecular weight of 198.22g/mol and are composed of one ethylene glycol molecule attached to two methacrylate groups as can be observed in figure 3.1. Polymers with methacrylate groups are known for their high glass transition temperature, tensile strength, stiffness, and low plastic deformation [21]. At 20°C, EGDMA has a viscosity of 3.2mPa·s and density of 1.05g/ml

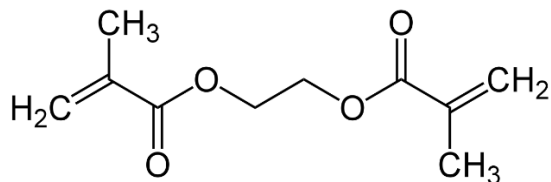


Figure 11 Ethylene glycol dimethacrylate molecule

3.1.2. Dispersant: Solplus D540

A commercial anionic dispersant, Solplus D540 was donated from Lubrizol Corporation (Wickliffe, USA). It was used to reduce viscosity by aiding the dispersion of HAp particles in EGDMA, as D540 polymer chains attached to the HAp surface and produced electrosteric repulsion. D540 has a density of 1.19g/cm³.

3.1.3 Photoinitiator: Diphenyl (2,4,6 trimethyl benzoyl) phosphine oxide

To trigger photopolymerization in the 3D printing process, diphenyl (2,4,6, trimethyl benzoyl) phosphine oxide (TPO) was added to the slurry. TPO chemical composition and molecular weight were C₂₂H₂₁O₂P and 348.37g/mol, respectively. The reagent had a 98% purity and was purchased from TCI America.

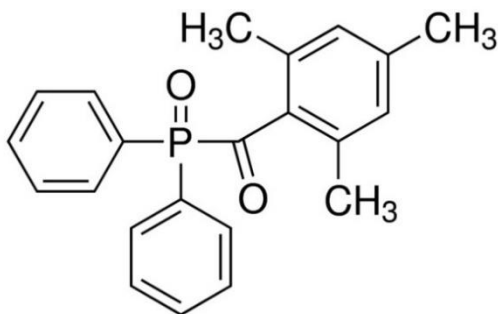


Figure 12. Photoinitiator molecule diphenyl (2,4,6, trimethyl benzoyl) phosphine oxide

As can be seen in figure 3.3.a TPO absorbance spectra have a wavelength range of absorption between 200-410nm with three maximum peaks in 235nm, 382nm, and 398nm [45,46]. The photon-induced cleavage reaction that produces a free radical to trigger photopolymerization is shown in figure 3.3.b.

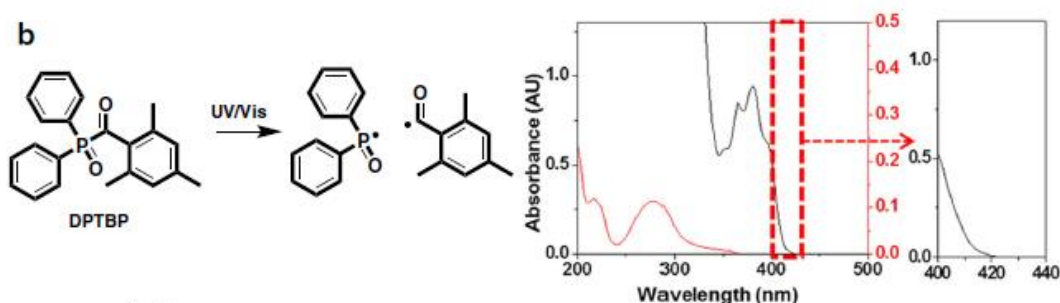
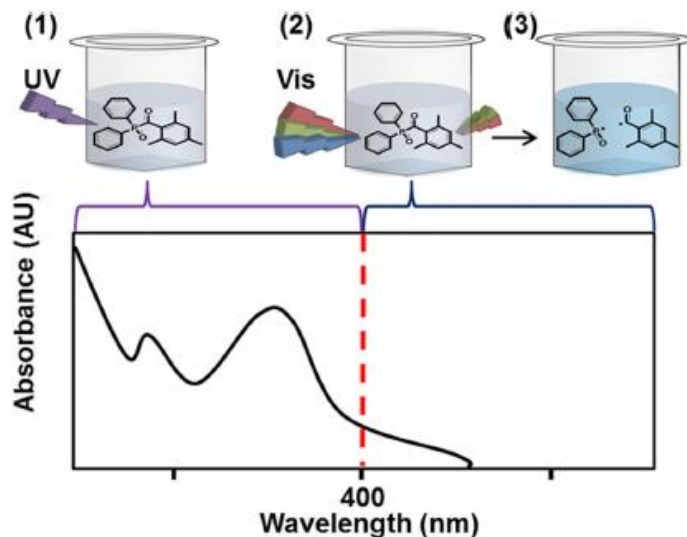


Figure 13. (a) absorption spectra of TPO upon UV and visible range irradiation. (b) TPO reaction mechanism: C-C bond undergoes in homolytic cleavage upon irradiation leading to two free radicals. Absorption spectra of TPO in function of wavelength where the red box represents the absorption in the visible wavelength[47]

3.1.4. Ceramics: Hydroxyapatite

Ceramic particle morphology plays an important role in rheological behavior, colloidal stability, and the sintering process of a resin. Achieving high solid content in the liquid phase depends on interactions between particles as well as between the particle and the solvent [48]. Therefore, it is important to control the morphology of the initial particles and understand the interactions previously mentioned. Two different HAp ceramic powders were pretreated; the initial physical properties are shown in table 2 and figure 3.4.

Table 2. Hydroxyapatite characteristics.

Hydroxyapatite Brand	Size	Specific Surface Area	Morphology	Reference
Macron	85.74±35.72nm*	67 m ² /g	Needle-like	Lopez-Ambrosio
Mk Nano	12µm	2-3m ² /g	Spherical	Vendor

The morphology of Mk Nano HAp (M K Impex Corp, Ontario, Canada) was spherical with minimal porosity, a particle size of 12µm and a specific surface area of ~3m²/g. In the case of Macron HAp (Macron Fine Chemicals, USA), the primitive particles were needle-like, 100nm in size, but these agglomerated and formed semi-spherical clusters of different sizes. Due to the small size of Macron HAp, the specific surface area was 67m²/g.

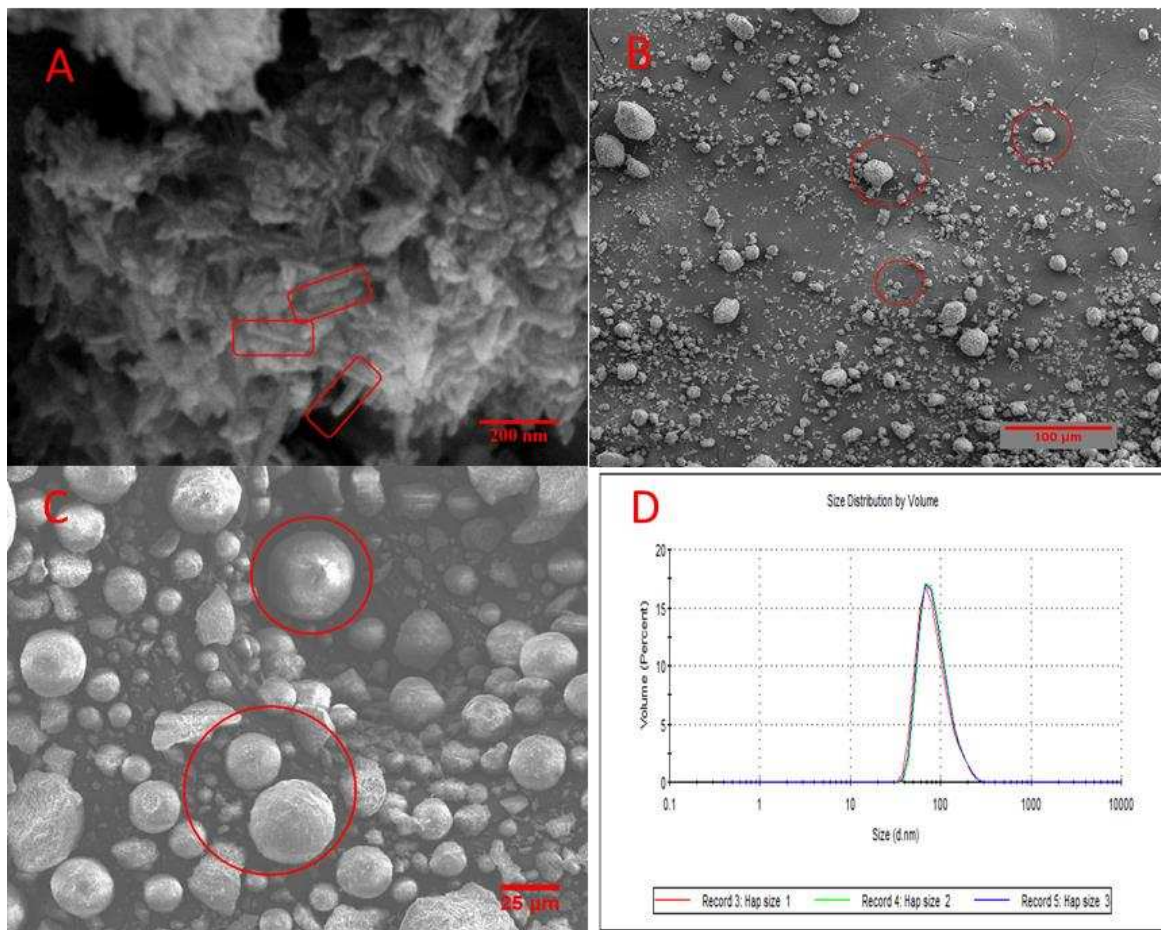


Figure 14. SEM images of as received HAp initial morphology. (A) Primitive particles of Macron HAp are pointed by red squares. (B) Agglomerates of Macron HAp with semispherical shape are shown with red circles. (C) Mk Nano HAp spherical shape is pointed with red circles. (D) Size distribution of Macron HAp.

In colloidal systems containing nanoparticles, Van der Waals attraction forces were higher due to the relatively high total exposed surface area of the particles. Therefore, larger quantities of dispersant are needed to stabilize the colloid.

3.2. Methods of HAp pretreatment

3.2.1. Method to increase the particle size of Macron HAp.

Sintering was chosen as the method to increase the particle size of Macron HAp and decrease the specific surface area. Two isotherm temperatures and two holding times were tested to assess the resultant increase in particle size. The isotherm temperatures were 700°C and 800°C, and the holdings time were 30min and 60min, respectively.

For each sample specified in table 3, 2g of Macron HAp were weighed and placed in an alumina crucible with lid. The crucible was situated in a high-temperature furnace (Thermolyne47900, Thermo Scientific). Starting at room temperature, the sample was heated and held in the temperature and time according to the treatment table 3 in air atmosphere. After, the sample was allowed to cool to room temperature and stored in a 20ml glass vial.

Table 3. Sample treatment to increase particle size.

Sample	Isotherm temperature [°C]	Holding time. [min]
A1	700	30
A2	700	60
A3	800	30
A4	800	60

The resulting Macron HAp particle sizes were characterized with scanning electronic microscopy (SEM, Jeol) and dynamic light scattering (DLS, Malvern Instruments).

For SEM analysis, the samples were attached to an aluminum sample holder using carbon tape, sputtered with 15nm of gold and imaged at 15kv to evaluate sample morphology.

For DLS analysis, 0.01g of HAp was mixed with a solution of 2 vol% of Darvan 821A (Vanderbilt Minerals LLC, USA) in DI water. Then, the aqueous solution was agitated in a vortex and filtered with 4 μ m filter paper. If the samples presented agglomerates or turbidity, DI water was gradually added until the solution was transparent. 1ml of the solution was then transferred to a polyacrylate cuvette for analysis.

3.2.2. Method to decrease particle size of Mk Nano HAp.

Preliminary studies done by the author aimed to use MK Nano HAp size as received in the production of slurries with a high content of HAp. However, in all trials, the particles of HAp agglomerated and flocculated. It was believed that the low surface area of the particles was not large enough to interact with the dispersant and the size was too big, so the gravity settled the particles. Therefore, high energy ball milling was used to decrease the particle size of Mk Nano HAp in a planetary ball mill (PBM, Across International). Two rotational speeds, two weight ratios (media: powder), and two milling times were tested to assess the decrease in particle size. The experiment conditions were rotational speeds of 300 rpm and 360rpm, media to powder ratios of 1: 1 and 1:2, and milling times of 2h and 4h respectively.

For each experiment, 2g of Mk Nano HAp were weighed and placed in a 50ml Teflon jars with the weight of agate media specified in table 4. The jars were sealed and loaded into the PBM. 50% duty cycles of 10min were programmed. Characterization of resultant Mk Nano HAp particle size was studied by SEM and DLS similarly as described in section 3.2.1.

Table 4. Conditions of experiments to decrease particle size

Sample	Rotational speed [rpm]	Weight ratio [balls:powder]	Milling times [h]
MK1	300	1:1	2
MK2	300	1:1	4
MK3	300	2:1	2
MK4	300	2:1	4
MK5	360	1:1	2
MK6	360	1:1	4
MK7	360	2:1	2
MK8	360	2:1	4

3.3. Resin formulation of 41vol% (67wt%) hydroxyapatite

HAp slurries were produced using a planetary ball mill. The slurries were mixed in Teflon jars with agate milling media to prevent vaporization of EGDMA and adhesion of the slurry to the walls of the jars. 27wt% EGDMA, 0.11wt% TPO, and 6.03wt% D540 were mixed in the PBM at 120rpm for 15min with the 10g of agate balls (ratio media: powder 2:1, approximately five balls of 1cm of diameter and five balls of 0.5cm of diameter. These parameters were chosen experimentally) until a homogenous slurry was formed.

HAp was gradually added to the solution. Three HAp additions were incorporated and mixed in a 10 min 50% duty cycle. In this context, 33.5wt%, 17wt%, and 16.5wt% of HAp were mixed at 300rpm for 2h, 320rpm for 2h, and 340rpm for 4h respectively.

Finally, HAp slurry was transferred to a syringe, wrapped in aluminum foil and kept in the dark until use. For more information, refer to Appendix 1.

Rheological behavior and viscosity of HAp slurries were studied in a parallel plate rheometer (TA Instruments). Approximately 1ml of HAp slurry was accommodated between two parallel plates of 2.5cm diameter with a stainless-steel spatula. Then, the parallel plates were moved together until a gap of 1.1mm was reached, and the sample was allowed to relax for five minutes. Then,

apparent viscosity was measured at 0.1s^{-1} , 1s^{-1} , 10s^{-1} , 100s^{-1} shear rates. This procedure is described in more detail in Appendix 2.

3.4. Production of complex HAp structures: (3D printing)

Additive manufacturing was used to build HAp structures. The 3D printer (Hyrel Engine SR, Atlanta, Georgia, USA) used in this project was equipped for viscous extrusion and with layer-wise photo-curing (405nm LED light source), as can be seen in figure 3.5. The printer precisely controlled movement in the three primary cartesian coordinates (x, y, z-axis) with a minimum mechanical resolution of $50\mu\text{m}$, $150\mu\text{m}$, and $10\mu\text{m}$ in x, y, z directions, respectively. The apparatus was accommodated with a light source attachment with three LED lights, unlike the ring shown in figure 3.5 that had tunable power density ranging from 0 to $2\text{mW}/\text{cm}^2$ and a mechanical extruder with an aluminum syringe coupled with a 0.413mm diameter and $\frac{1}{2}$ inch length nozzle. The to-be-printed structures were modeled in Computer Aid Design (CAD) using SolidWorks (Dassault Systèmes) and saved as .STL files or downloaded from the community MakerBot website (<https://www.thingiverse.com/>). After, the designs were sliced using the open source 3D printing software Slic3r (<https://slic3r.org/>) with the following settings: print speed of $300\text{mm}/\text{min}$, layer height of 0.4mm or 0.3mm , line width of $\sim 0.4\text{mm}$, infill percentage and pattern were chosen depending on the design. The light power density was set between $0.7\text{ mW}/\text{cm}^2$ - $1.3\text{ mW}/\text{cm}^2$ depending on the cross-sectional diameter of the structure in the 3D printer software Repetel (Hyrel, Atlanta, Georgia, USA).

To obtain a steady flow of the resin through the nozzle, three skirt loops were printed prior to building up the shapes, layer by layer. An exothermic photopolymerization reaction was initiated by continuous exposure to the light source, causing a polymerized cross-linked network that

increased viscosity and hardened the structures. When the printing process finished, the green bodies were exposed again to the light source with a power density of 100% for 5min so the last layer has the same irradiation time as the previous layers. Finally, the printed structures were preserved in the dark at room temperature.

The homogeneity of HAp dispersion in the EGDMA was assessed after the 3D printing process where the particles were immobilized by the crosslinked polymer. Elemental composition of carbon, oxygen, calcium, and phosphorus in the green bodies was obtained by energy-dispersive X-ray spectroscopy (EDS) where the distribution of the elements on the surface of the samples could be imaged. For accuracy and better detection of the characteristic X-ray emission of the elements, the samples were polished to a maximum defect of 15 μ m with 1200 grit sandpaper. For more information for the polishing process, refer to Appendix 3.

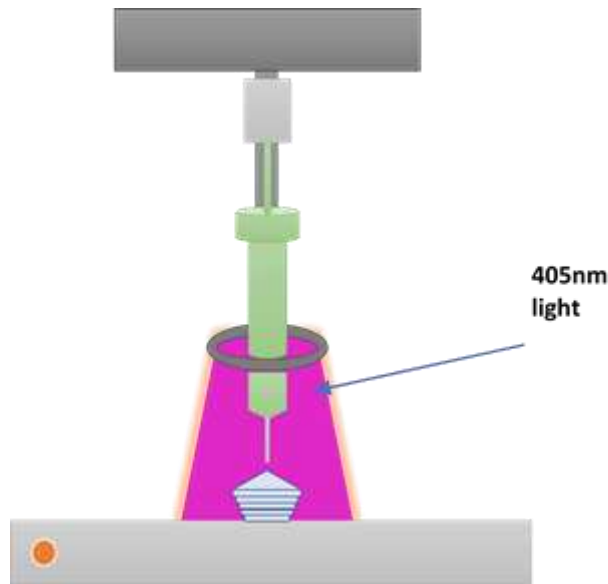


Figure 15. Schematic of the 3D printing process.

3.5. Sintering of HAp complex structures

After 3D printing green bodies of HAp, a process of densification was applied to eliminate the polymeric support material (P-EGDMA) and consolidate the HAp particles in the samples. Conventional pressureless sintering in air atmosphere was performed in a high-temperature furnace. A two-step sintering method was used to densify the HAp samples. Sintering profile is shown in figure 3.6.

A 3^2 design of experiments (DOE), for a total of 9 experiments (see table 3.4.), with four replicates, was carried out to assess the resultant relative density, average grain size, and volumetric shrinkage of HAp samples. In the DOE, the experimental factors were heating rate (T2, 5, 15, 25 °C/min) and holding time (H2, 2, 3, 5 hours).

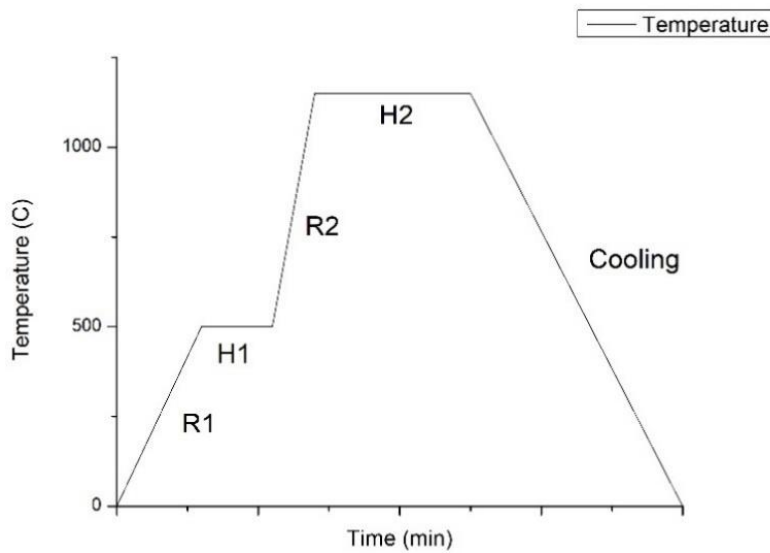


Figure 16. Sintering profile used to densify HAp structures. R1 and R2 are heating rates, and H1 and H2 are holding times

HAp green body slabs were 3D printed with 15mm x1.60mm x 10mm dimensions, sintered according to the conditions specified in table 5 and sonicated for one hour in 99 vol% ethanol.

Table 5. DOE sintering varying T2 and R2.

Sample	Heating Rate (R2) [°C/min]	Holding time (T2) [h]
5R2H	5	2
5R3H	5	3
5R5H	5	5
15R2H	15	2
15R3H	15	3
15R5H	15	5
25R2H	25	2
25R3H	25	3
25R5H	25	5

The crystalline phase was studied by X-ray diffraction (XRD, Davinci D8) and the relative density by the Archimedes method. The average grain size was measured following the standard ASTM E112 using Image J software (NIH, Maryland) on SEM images.

For XRD studies, sintered samples were sonicated in ethanol and then ground to a powder with an agate pestle and mortar. Then, the powder was analyzed with $\text{CuK}\alpha$ radiation in a scan range from 20° to $60^\circ 2\theta$, step size of 0.02° and scan rate of $2^\circ/\text{min}$.

Relative density was measured using the Archimedes method. Sintered HAp samples were weighed in air, then the samples were coated with a super acrylic coating (Sally Hansen, USA) and weighed in air again. Finally, the coated samples were submerged in DI water and weighed. A reference density of $3.14\text{g}/\text{cm}^3$ (specified by the manufacturer) was used for fully dense HAp in the Archimedes method comparison.

After sintering, due to the coalescence of HAp particles and the decomposition of PEGDMA, the sample size decreased (shrinkage). Dimensional shrinkage was obtained by measuring the dimensions of the slabs before and after sintering with a digital caliper.

Preliminary studies determined that the first heating rate (R1) in the sintering process should not be faster than 5°C/min because rapid heating caused defects due to the rate of burning and degassing of the polymer as can be visualized in figure 3.6.a. Moreover, the first isotherm temperature (T1) was required to allow the polymer matrix to decompose and outgas. T1 was determined by thermogravimetric analysis (TGA, TA Instruments, USA). This is shown in figure 3.6.b, which indicated the temperature at which the polymer burned out and HAp densification began.

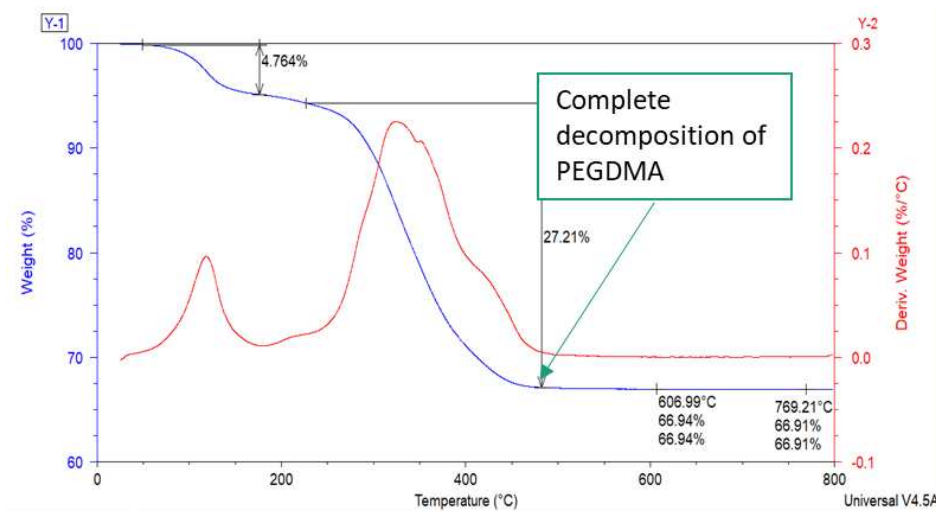
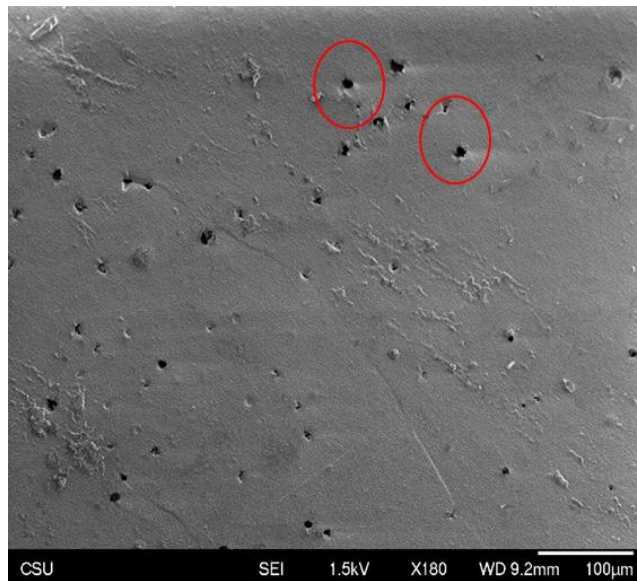


Figure 17. (A) SEM image of HAp densified surface using a heating rate (T1) faster than 5°C/min. Red circles show defects created by rapid degassing of burned PEGDMA. (B) Thermograph of HAp green body shows where total decomposition is reached ~450°C.

3.6. Flexural strength

Flexural strength and flexural modulus of green bodies and sintered HAp were studied. All samples for this testing were 3D printed on a sticky double-sided gel tape 1.3mm thick (Gorilla Glue Company mounting tape, Ohio, USA), to attach the to-be-print sample to the printing bed and then to avoid cracks in the detachment process. Rectangular samples 4mm x 4mm x 20mm were 3D printed using the following settings: linear pattern, 100% density infill, and a layer height of 0.3mm. After printing, the surfaces were polished with 800 and 1200 grit sandpaper to obtain smooth surfaces with a maximum defect size of 15 µm. For more information for the polishing process, refer to Appendix 3.

A custom 4 point bending tester developed by Aguirre et al. [49] coupled to an Instron testing machine (Instron model 8501) was used to test the flexural strength of the samples according to the ASTM C1161 and ASTM D7264. A 1kN load cell with a crosshead displacement rate of 0.1mm/min was used for the tests. The stress (σ) and strain (ε) were calculated as follows:

$$\sigma = \frac{3PL}{4bd^2} \quad (2)$$

$$\varepsilon = \frac{4.36\delta h}{L^2} \quad (3)$$

Where P, L, b, δ , and d were the force, inner span length, specimen width, displacement, and specimen thickness, respectively. The samples were tested perpendicular to the build Z direction,

as is shown in figure 3.8 for consistency in the results because isotropy properties of the structures have not yet been proven.

Seven green bodies and seven sintered HAp samples were used to determine the flexural modulus and strength.

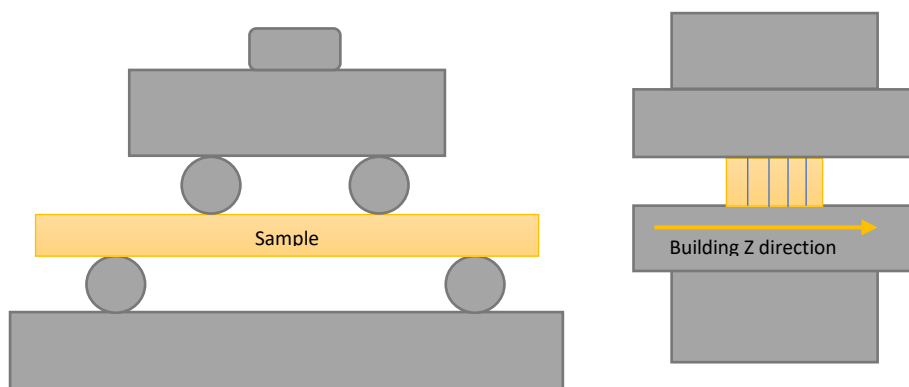


Figure 18. (A) Front view of flexural 4-point bending tester. (B) Lateral view of flexural 4-point bending tester. Testing direction for the samples was perpendicular to the building direction.

3.7. Cytotoxicity studies

The biological response and measurement of cell damage of sintered HAp structures were assessed by a leaching study following ISO 10993:51, Biological Evaluation of Medical Devices Part 5: Tests for *in vitro* cytotoxicity. Adipose-Derived Stem Cells (ADSCs) derived from rats, were used for this test.

Lactate Dehydrogenase (LDH) is created during cellular production and is released to the media if cells die (i.e., if cell membranes rupture). Therefore, by measuring the level of LDH in the medium, it is possible to determine the cytotoxic response (i.e., quantify the amount of cell death) resulting from the presence in the media of HAp structures. Four HAp samples were tested (n=4). Lysis buffer was used as a positive control due to its ability to kill cells. As a negative control, spontaneous LDH produced by cell proliferation on tissue culture polystyrene was measured from fresh media.

HAp samples were crushed with an agate pestle and mortar and sterilized using UV light. Growth media was composed of 85 vol% α -MEM, 10 vol% FBS, and 1% pen/strep. Each sample was submerged in 3 ml of growth media in a scintillation vial and incubated at 37°C and 5% CO₂. Three measurements of LDH levels in each vial were made at 7, 14, and 28 days, as follows.

At each time point, 1 ml of media containing seeded ADSCs was transferred to a 48 well plate. In each well, 10,000 cells were confined. Extracts with cells were incubated for 24h. The next day, the LDH level was measured in a plate reader (FLUOstar, Omega, BMG Labtech, Durham, NC). The absorbance of the sample was measured at 490nm and 680nm. Then, LDH activity and percent cytotoxicity were obtained by applying the following equations:

$$LDH\ HAp\ activity = (LDH\ absorbed\ at\ 490nm) - (LDH\ absorbed\ at\ 680nm)$$

$$\% \text{ Cytotoxicity} = \frac{LDH\ HAp\ activity - Spontaneous\ LDH\ activity}{LDH\ activity\ positive\ control - Spontaneous\ LDH\ activity} * 100$$

3.8. Statistics

Analysis of variance (ANOVA) and Tukey tests were performed for the experiments using software Origin 8.5 at a 95% significance level (p<0.05).

4. RESULTS AND DISCUSSION

All the results of the different methods and characterizations described in section 3 are presented in this section. Moreover, discussion and analysis of the results will be provided in detail.

4.1. Pretreatment of HAp

Size and surface area of the particles of HAp have an active role in the dispersion stability and viscosity properties of a resin [48]. When particles have extensive surface areas, Van der Waals attraction forces are stronger favoring the agglomeration and flocculation of the dispersed particles in the liquid. Thus, to counter the attractive forces, additional quantities of dispersant must be added to cover the extensive surface areas and equilibrate the forces. In the case of this project, electrosteric forces produced by D540 Solplus dispersant were used to stabilize the dispersion. Moreover, the flowability of the resin is also a function of the aspect ratio of the dispersed particles. Therefore, by using needle-like particles, the flowability properties of the resin were lower [26]. Thus, pretreatment of HAp particles to modify surface area and morphology were investigated.

4.1.1. Increasing particle size of Macron HAp

Macron HAp had a specific surface area of $67\text{m}^2/\text{g}$, size of $\sim 86\text{nm}$, and needle-like morphology. A change in morphology of HAp particles (increase in size and decrease in specific surface area) was desired to produce HAp slurries with lower viscosity.

A change in morphology was successfully achieved by a heat-treatment process. Needle-like primitive particles of HAp (figure 4.1.a) coarsened into semi-spherical shaped grains as is shown in figure 4.1.b. This process led to a slight increase in particle size but did not lead to a significant decrease in surface area due to the porous morphology. While the formation of particles with aspect ratio closer to one was promising for improving flowability properties, preliminary results from

this study found that the heat-treated powders decreased the viscosity in the slurries, but ultimately were unstable and flocculated in the EGDMA. At this time, it is believed that the heat-treated powders were unstable as they were sintered agglomerates with relatively high mass compared to the non-treated powders. Additionally, dispersant could enter the porous structure of the sintered agglomerate and act like deadweight. Given these two factors, it is likely that these powders would sink.

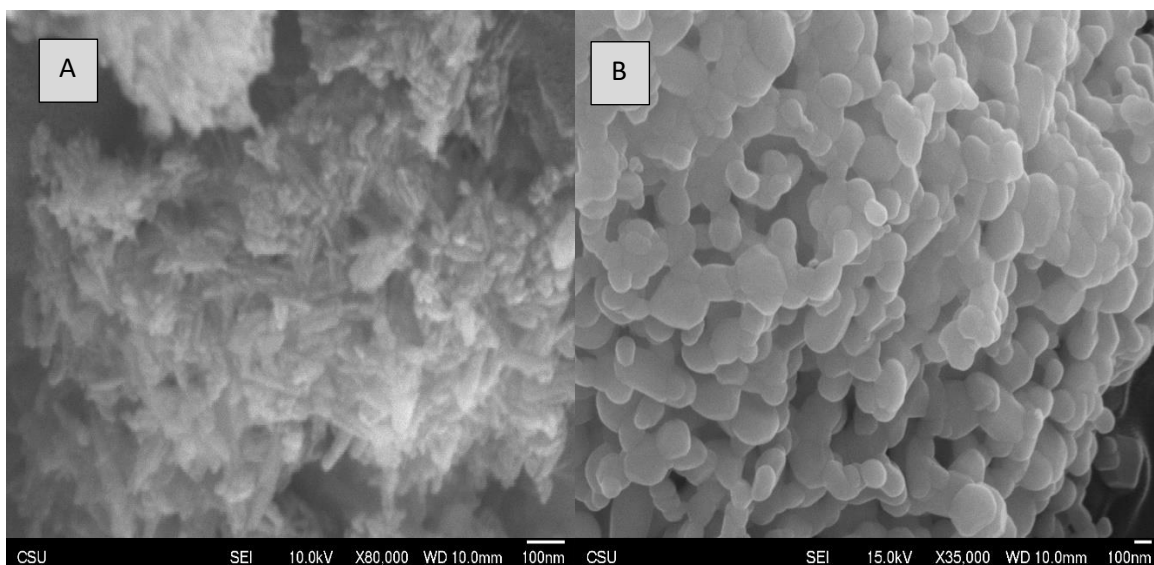


Figure 19.(A) As received Macron HAp particles. (B) Macron HAp after thermal treatment.

4.1.2. Decreasing particle size of MK Nano HAp

MK Nano HAp had a specific surface area of 2 m²/g, a size of 12μm, and spherical morphology. A higher surface area around 12 m²/g was desired to allow electrosteric stabilization to occur between the particles and the medium with low dispersant addition without flocculation [48]. To achieve this, the as-received MK Nano HAp particles were crushed in a PBM at different milling speeds, times, and the weight ratio of media-to-powder. Due to the brittle nature of hydroxyapatite, this process was unfavorable for the spherical morphology of the powders as is shown in figure 4.2.B. At longer milling times, the particles lost spherical shape and their size decreased

excessively, as discussed in the following paragraph. DLS measurements (see figure 4.3) indicated that a bimodal size distribution was obtained after 2h milling time with particle sizes of $30.4\pm 12.65\text{nm}$ and $161\pm 69.99\text{nm}$, while a monomodal size distribution was obtained after 4h milling time with a particle size of $51.10\pm 36.08\text{nm}$.

In volume, most of the resulting particles in all trials, regardless of milling time and milling speed were smaller than 100 nm. This increased the difficulty of mixing pretreated MK Nano HAp with EGDMA, even when mixed in low vol% increments. Furthermore, the slurries dried overnight. These phenomena may be attributed to the excessive surface area of the particles, which leads to a higher energy system. Thus, more additions of dispersant must have been necessary to stabilize the system, but if more dispersant were added, the viscosity would have increased due to the intrinsic viscosity of the dispersant. These results led to a Photopolymeric system that was not 3D printable.

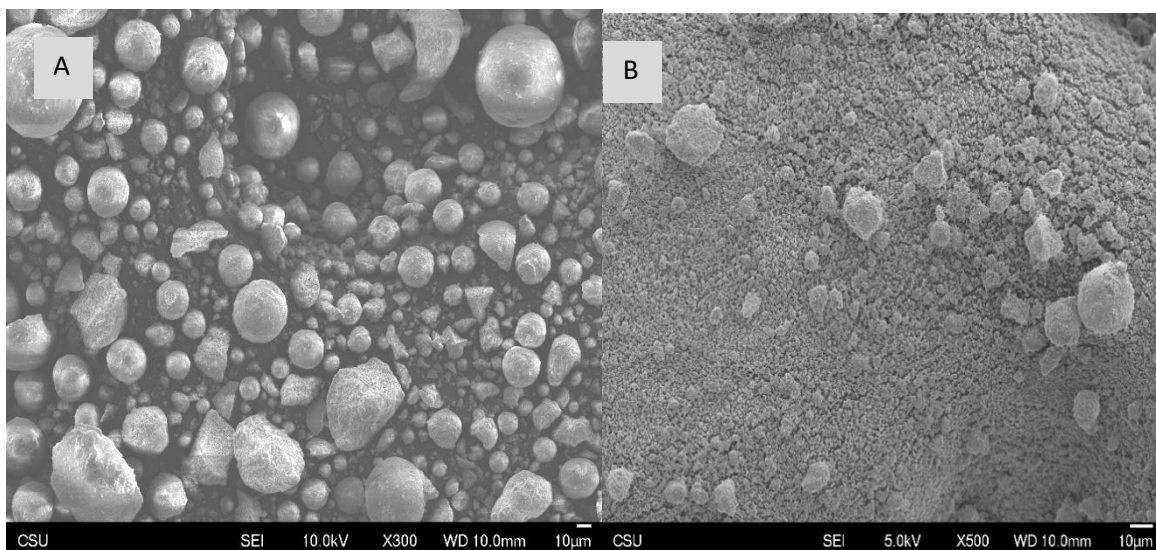


Figure 20. (A) As received MK Nano HAp particles (B) MK Nano HAp particles after ball milling treatment for 2h.

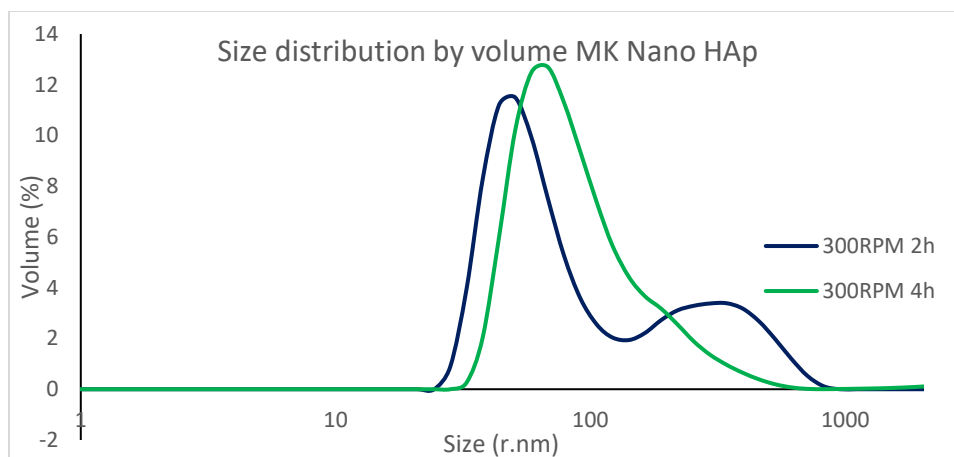


Figure 21. Particle size MK Nano HAp after ball milling treatment milled at the same speed and ball-to-powder ratio. Green line represents sample ball milled for 2h, and dark blue represents sample ball milled for 4h.

4.2. Resin formulation

Macron HAp as received was used in the resin formulation because pretreated powders mentioned above (see section 4.1) were not stable and flocculated when suspended in EGDMA. Preliminary work discovered that 41vol% as received Macron HAp slurries in EGDMA could be obtained. However, this process was time-consuming (48h) and difficult to standardize because the slurry was made by hand-mixing the components while adding the HAp in 1g increments. This approach helped to minimize the agglomeration of HAp particles but the viscosity of the slurry and degree of mixing increased exponentially. To overcome this, a new approach to the formation of 41vol% HAp slurries was developed.

PBM was chosen to enhance the production of HAp slurries. Normally, PBM is used to modify particle size distribution of a powder as it is crushed between two hard surfaces of milling balls [50]. However, when this tool is used for mixing with liquids, slower milling speeds, and fewer quantities of milling media are necessary [48]. PBM enabled the production of homogenous slurries in a time frame of 8h. Different parameters, including the ball-to-powder weight ratio,

mixing speed, and HAp additions, were assessed by trial and error. The flowability of the slurry and homogeneity were used to choose the best parameters.

It was found that 41 vol% of HAp slurries could be produced by mixing the components with parameters specified in section 3.3 without modifying HAp particle morphology. The mass of HAp had to be added in a minimum of three steps because if fewer steps were used, the monomer evaporated causing hardening in the slurries as the HAp particles were too close to each other, could not wet properly and the temperature of the system raised. Besides, The jars did not have enough space for the media, powder, and liquid to tumble effectively. The jars should have an empty space between 10% to 25% to work properly [50]. Moreover, the mixing speed had to be lower than 400RPM to allow mobility of the slurry when the viscosity of the HAp slurries increased, so the milling speed had to be suitable for the milling balls to not stick on the walls or bottom of the jar [50,51]. A failed attempt to produce a HAp slurry is shown in figure 4.4, where the slurry hardened before adding 25 wt% of HAp to complete 67 wt% HAp slurries.

The volume of the milling media occupied ~10% or less of the jar which produced a low number of collision. Furthermore, Smaller particles are stronger (nanometric size) than bigger particles and do not breakdown as easy, so HAp particle morphology was not modified in the mixing process [51].



Figure 22. Dried HAp resin in milling jar with black agate milling balls.

4.2.1. HAp resin viscosity and homogeneity

Rheological behavior of 41 vol% HAp slurries is presented in log-log scale graphs. In figure 4.5 a significant decrease in the apparent viscosity (η) was observed as the shear rate ($\dot{\gamma}$) increased. Moreover, for 0.1 s^{-1} shear rate, an initial shear stress was necessary to begin deformation. These phenomena are typical of shear thinning fluids with viscoplastic behavior.

The apparent viscosity obtained by the different shear rates tested in a parallel plates setting obeyed the Ostwald de Waele (Power-Law) equation.

$$\eta = m(\dot{\gamma})^{n-1}$$

Where m represents the consistency of the slurry in units of MPa.s, and n is the power-law index of the shear thinning behavior of the fluid. The power-law index can take values between $0 < n < 1$ where the smaller the n value, the higher the shear thinning behavior of the fluid [52].

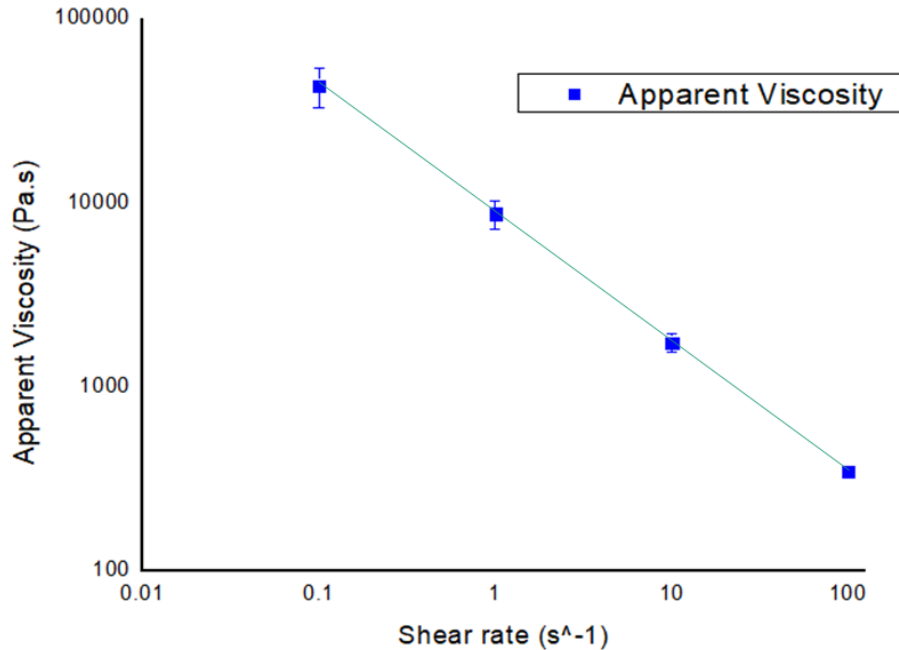


Figure 23. Shear thinning rheological behavior of HAp slurries.

For 41 vol% HAp slurries, m and n values were $m = 9862.96 \pm 1610.23$ MPa.s and $n = 0.3 \pm 0.023$ with an $R^2 = 0.99 \pm 0.003$. The variability in the consistency (m) could be a result of the temperature change in the room at the moment of testing, and the resistance of the needle-like HAp particles to flow. The viscosity of a slurry is dependent on the morphology of the dispersed phase; thus, the asymmetric needle-like particles may affect the consistency of the slurry. The more the particles deviate from spherical symmetry, the more the viscosity increases because asymmetric particles gain more kinetic energy that dissipates with the applied force that resulted from the shear rate [26]. This has an obvious effect on 3D printability, especially of complex structures, as discussed in section 4.3.

The rheological behavior of the HAp slurries as a function of storage time was studied. It was desired to quantify possible drastic changes in viscosity due to its light-sensitive nature and other storage conditions. Therefore, apparent viscosity as a function of shear rate was measured over 20 days. This is shown in figure 4.6.

For each shear rate, it was found that there was not a significant difference at $p < 0.05$ in apparent viscosity for the days in which the measurements were taken. However, a small trend of increasing apparent viscosity is observed in figure 4.6, most noticeable on day 20. Hence, it was hypothesized based on the statistical analysis that the storage conditions effectively prevented exposure to light, possible photopolymerization reaction and evaporation of EDGMA of HAp slurries but they should be keeping in storage for less than 20 days.

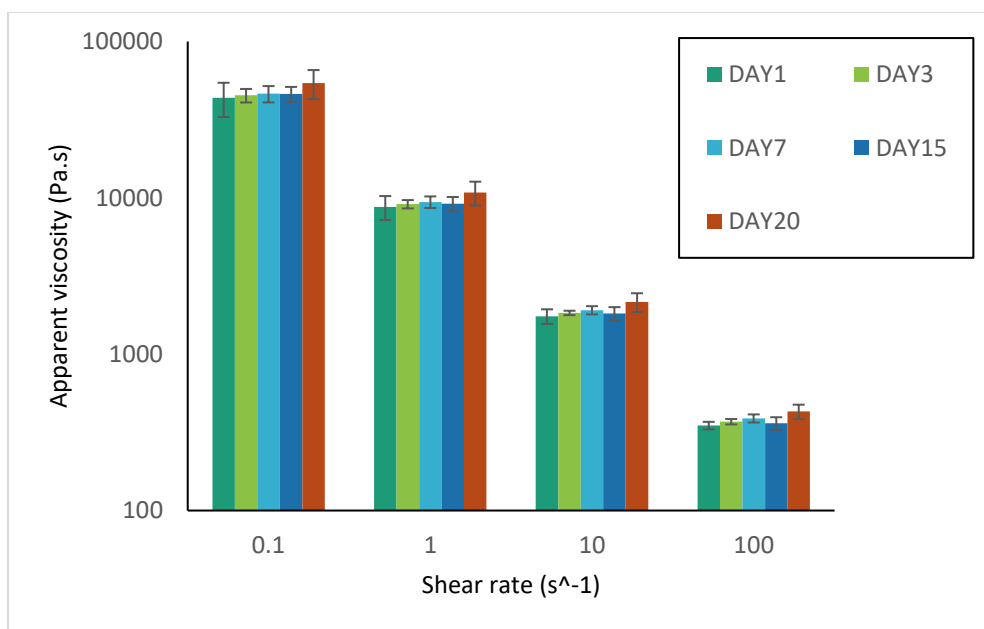


Figure 24. Viscosity of HAp slurries during the first 20 days after synthesis.

Moreover, the homogeneity of the slurry was studied by assessing the distribution of the elemental composition of carbon, oxygen, calcium, and phosphorus in the green bodies. For accuracy and better detection of the characteristic X-ray emission of the elements, the samples were polished up to a 15 μ m defect with 1200 grit sand paper. Smoother surfaces were not possible to obtain due to the brittleness of the samples. It is recommendable that the surface roughness of the samples to be lower than 15 μ m to assure alignment with the EDS detector.

Figure 4.7 shows a micrograph of the surface and elemental maps of a green body of HAp. Equal distribution of oxygen, calcium, carbon, and phosphorus can be observed in the elemental maps through all the surface independently of the surface roughness. Additionally, line scans were performed on the surface of the green bodies, and no significant changes in the characteristic emission of the elements were evident. This is shown in figure 4.8.

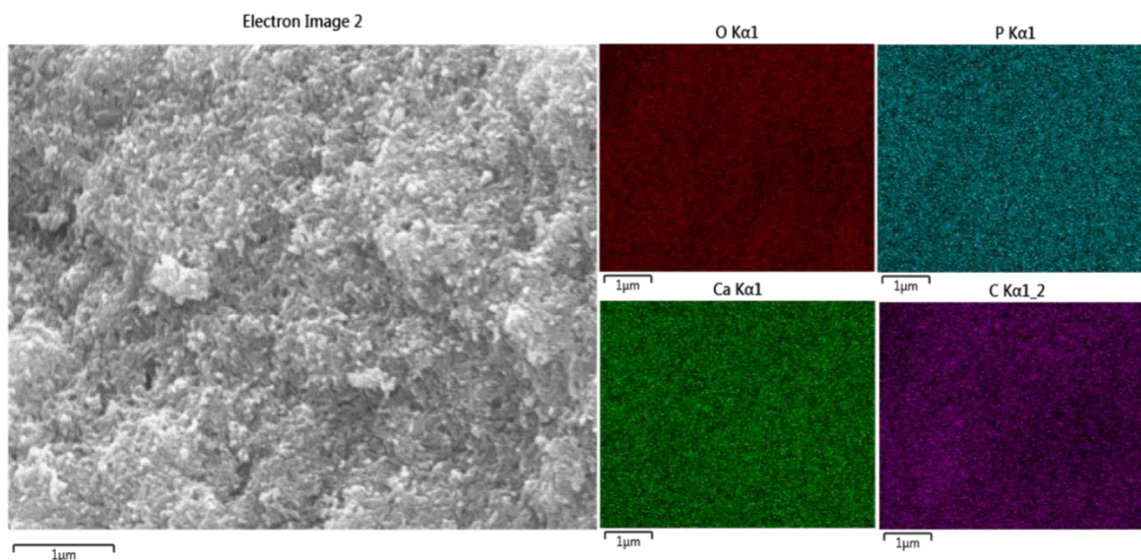


Figure 25. SEM image of HAp/PEGDMA green body surface. Lines are the product of the polishing process. Elemental maps of phosphorus, calcium, carbon, and oxygen are presented in green, blue, purple, and red, respectively.

These analyses proved that the HAp was evenly dispersed in EDGMA when using a planetary ball mill and that the homogeneous dispersion was maintained after printing the structures. Pressure applied by the syringe plunger in the 3D printing process was not enough to break the electrosteric forces created by D540. Thus, HAp particles do not agglomerate and clog the nozzle and maintain the dispersion in the printed structures after 3D printing.

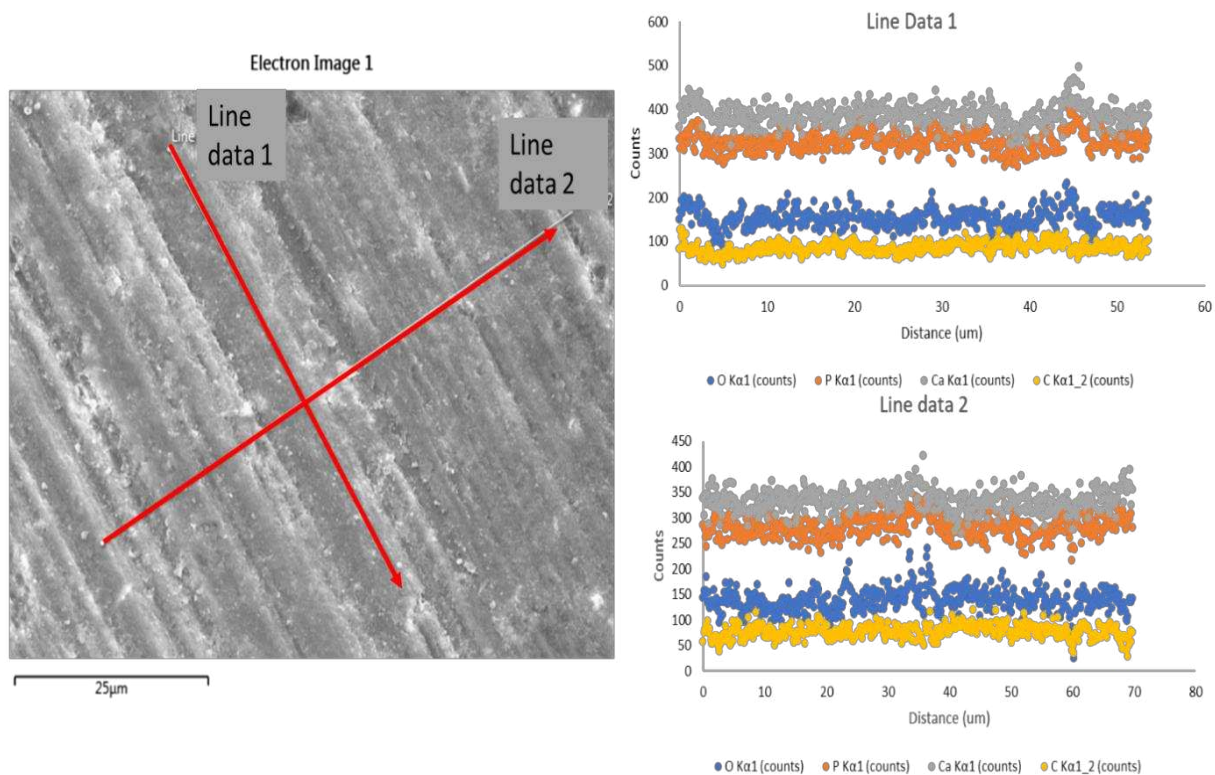


Figure 26. SEM image of HAp/PEGDMA green body surface. Red lines represent line scan of elemental composition done by EDS. Line data 1 and line data 2 show no significant change in element signal through the line scan length.

4.3. Production of complex HAp structures

Complex structures of HAp were successfully built with a combination of viscous extrusion and layer-wise photo curing techniques. Concave and convex shapes, interconnected pores, hollow and dense structures, were built with 41 vol% HAp slurries without the use of support materials (free form). Some examples are shown in figure 4.9.

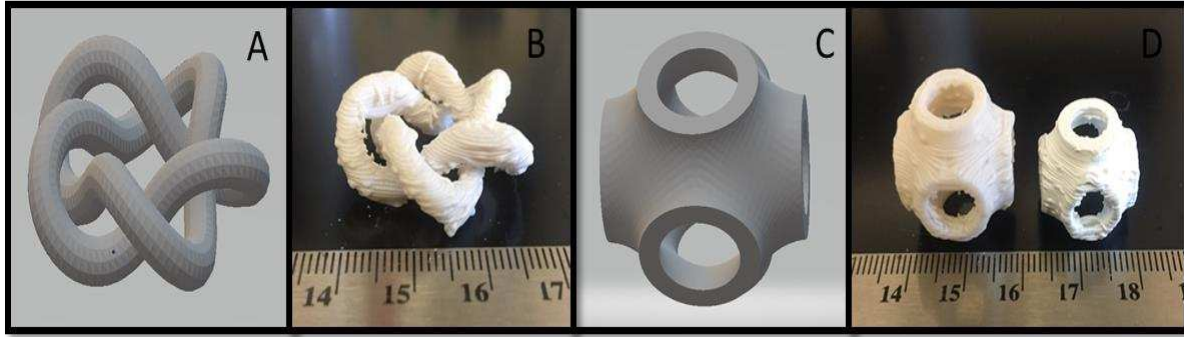


Figure 27. 3D printed complex structures. (B) and (D) are HAp complex structures produced from STL files (A) and (C), respectively. (D) contains a green body on the left and a sintered body on the right.

As a 3D printing method, viscous extrusion and layer-wise photo-curing were a suitable combination. Viscous extrusion allowed the production of structures from a slurry of high-volume content of solids. Photopolymerization solidified the material in a specific shape while offering the opportunity to avoid support structures in a free form.

The production of complex structures was enabled by the rheological behavior of the slurries and the 3D printing method. The shear thinning behavior of the slurries permitted control of the flow rate to deposit material when pressure was applied. For instance, on the one hand, if the slurries had Newtonian behavior, the free movement of the slurries would not have allowed using viscous extrusion, and the deposited roads would not have stayed in place. On the other hand, if the slurries had a shear thickening behavior, after applied stress, the nozzle would have clogged. Moreover, due to the high viscosity of the HAp slurries (paste-like) common 3D printing techniques such as stereolithography were not possible to use.

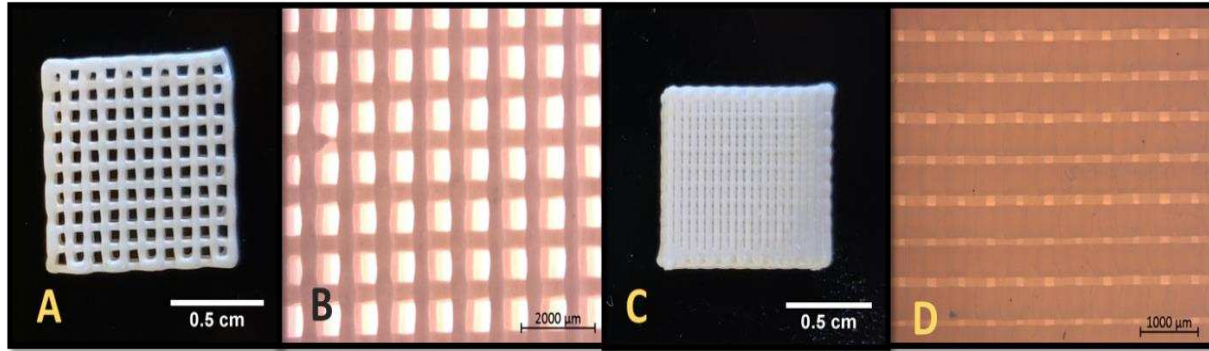


Figure 28. HAp/PEGDMA scaffolds (A) and (B) have $\sim 600\mu\text{m}$ pore size, (C) and (D) have $\sim 130\mu\text{m}$ pore size

An inner nozzle diameter of 0.413mm was used to produce highly detailed scaffolds with controllable pore features. Some examples with uniform square pore shape are shown in figure 4.10. The first scaffold (figure 4.10.A, B) had a pore size of $\sim 600\mu\text{m}$ and 40% porosity, while the second (figure 4.10.C, D) had a pore size of $\sim 130\mu\text{m}$ and 10% porosity. Other pore sizes, shapes, and porosities in scaffolds were successfully created with 41vol% HAp slurries that range in the parameters for the support and proliferation of cell growth [53]. In a broader context, 3D printing 41vol% HAp slurries using a combination of viscous extrusion and with layer-wise photo-curing techniques is promising for the creation of complex HAp scaffolds for orthopedic applications. These techniques combined overcame challenges of 3D printing complex structures, high-resolution structures with viscous slurries.

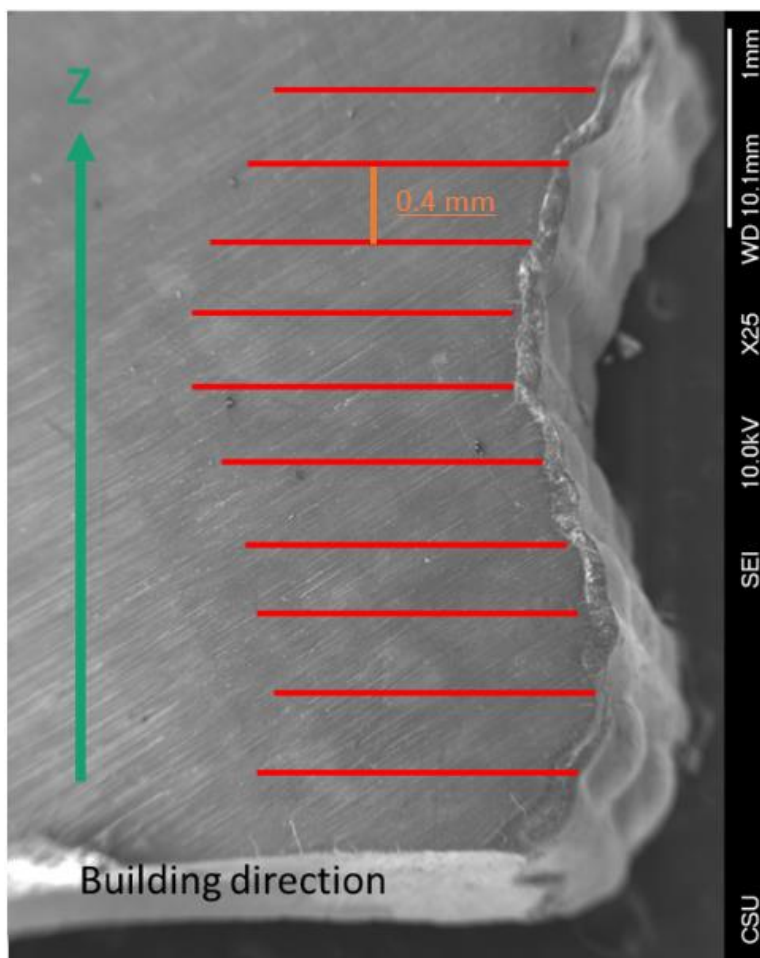


Figure 29. Layer cohesion of HAp samples. Red lines represent the location where layer division should be located, and the green arrow shows the building direction of HAp sample in the 3D printing process. The imaged face was polished, as described in Appendix 3.

No layer differentiation could be seen in the cross-sectional view of 3D printed samples, demonstrating complete cohesion between layers. This can be seen in figure 4.11. The red lines represent the locations where layer divisions would be located. Complete bonding between layers is achieved as irradiation of the first printed layer initiates the polymerization of EGDMA, but polymerization has not completed by the time the next layer is deposited. Therefore, the macroradicals from the previous layer have the mobility and reactivity to connect with the polymer chains of the layer above them. Moreover, the curing depth possibly penetrates more than two layers aiding the layer cohesion because the diameter of the light source covered all the x-y axis

cross-sectional area of the structures. In other words, the light source covers all the layer simultaneously.

4.4. Sintering of HAp complex structures

A representative X-ray diffraction pattern obtained for HAp sintered structures is presented in figure 4.12 and was characteristic for all samples obtained in the DOE. After the sintering process, the HAp samples presented three crystalline phases. The primary phase was HAp. The second phase corresponded to a small decomposition of HAp to β -TCP. The third phase belonged to a small contamination phase of gehlenite ($\text{Ca}_2\text{Al}(\text{AlSiO}_7)$).

It was hypothesized that the gehlenite phase was formed because some of the calcium of HAp reacted with aluminum and silicon from the furnace lining. The contamination reaction could have been triggered by the oxidation of old heating elements that pulled oxygen from HAp and favored the reaction between calcium, silicon, and aluminum.

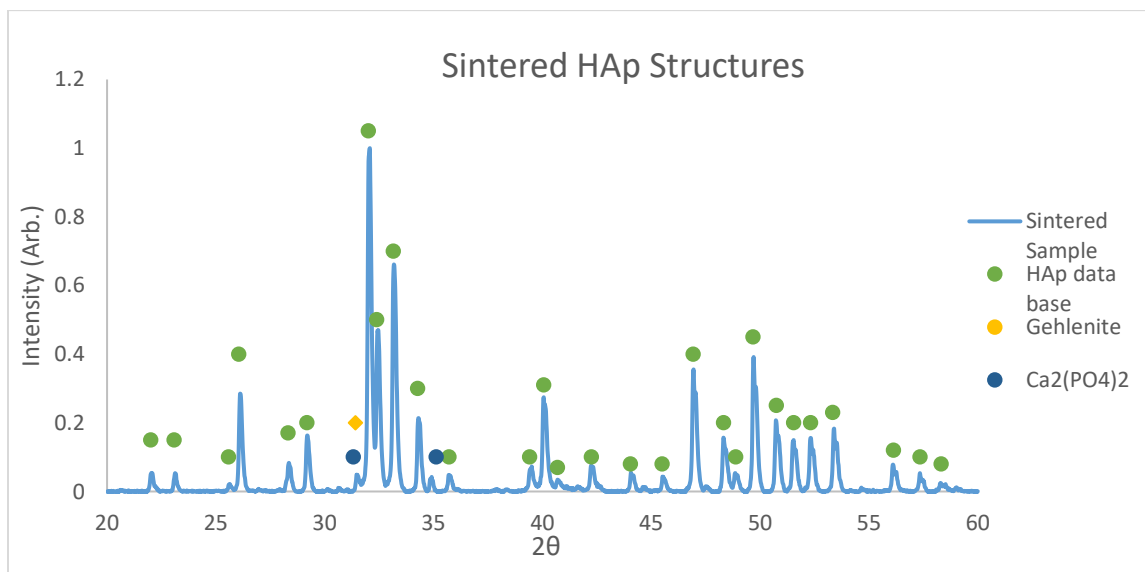


Figure 30. X-ray diffraction pattern of HAp sintered structures. Light blue is the data collected from the sample. Green, yellow and dark green are XRD data from the database of HAp, gehlenite and β -TCP, respectively.

Table 6 shows the average grain size and Archimedes density obtained for every sample in the DOE in addition to a preliminary experiment performed with a heating rate (R2) of 15°C/min and holding time (H2) of 3h at 1200°C.

Table 6. Sintering DOE

	Average grain size [μm]	Standard deviation [μm]	Archimedes relative density [%]	Standard deviation [%]
5R2H	0.417	± 0.057	69.591	± 0.881
5R3H	0.442	± 0.044	67.631	± 1.839
5R5H	0.503	± 0.037	68.811	± 0.738
15R2H	0.451	± 0.031	71.284	± 1.856
15R3H	0.532	± 0.071	73.495	± 1.065
15R5H	0.567	± 0.086	74.207	± 2.157
25R2H	0.198	± 0.015	58.173	± 1.672
25R3H	0.440	± 0.049	69.525	± 1.483
25R5H	0.485	± 0.056	72.640	± 1.586
1200°C15R3H	1.32	± 0.47	78.90	± 2.068

Although the sintering temperature of 1200°C produced samples with higher relative density compared to the samples sintered at 1150°C, lower temperatures were selected for the DOE due to the limited capabilities of the furnace. The necessity for holding high temperatures for more than 2h was not recommended by the furnace manufacturer. Moreover, at 1200°C, the average grain size obtained was at least three times larger than for the samples sintered at 1150°C, which could have a significant impact on the mechanical strength of the samples.

For the samples sintered with heating rate T2= 5 °C/min and different holding times (H2), grain size increased about $\sim 0.04\mu\text{m}$ for each extra hour that the sample was exposed at the high temperature. However, interestingly a correlation in densification could not be determined.

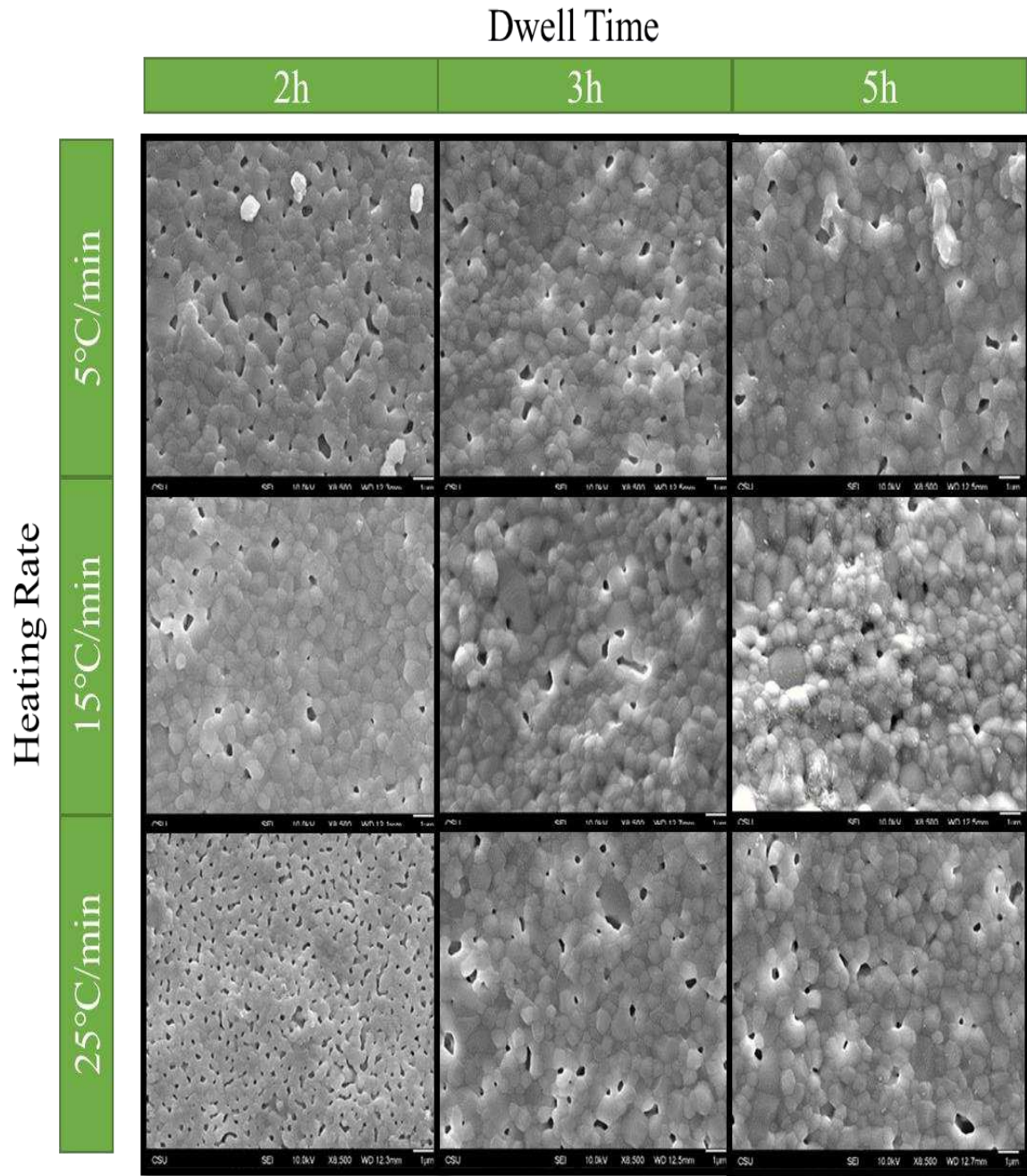


Figure 31. SEM images of surface densification of HAp samples resultant from the sintering DOE experiment.

Micrographs of the sintered HAp samples are shown in figure 4.13. These micrographs correspond to the top surface of very thin samples at 8500x magnification. It is observed that all the samples obtained homogenous microstructures. This is due to the use of two-step sintering [54]. The first

temperature ramp and isothermal hold served multiple purposes. In the first step, the PEGDMA was burned out of the sample as confirmed by XRD and EDS. In the second step, the finer HAp particles were absorbed into, the larger particles by surface diffusion mechanisms. This minimized density gradients in the sintered parts, as otherwise, the smaller particles would have densified before the larger particles [54]. Additionally, all the samples with exception 25R2H presented closed porosity in forms of circular or elongated pores leading to the belief that all the samples reached the third stage of sintering. For the case of 25R2H, the microstructure is similar to the second stage of sintering, which indicates that the samples did not have enough time to densify due to the fast heating rate and short holding time.

From the DOE it is concluded that HAp structures sintered with the same heating rate (R2) but different holding times (T2) showed a statistical difference in the average grain size but not in relative density except the sample R25H2. This is shown in figure 4.14. Moreover, HAp sintered samples with different R2, but identical T2 had significantly different relative densities ($p < 0.05$).

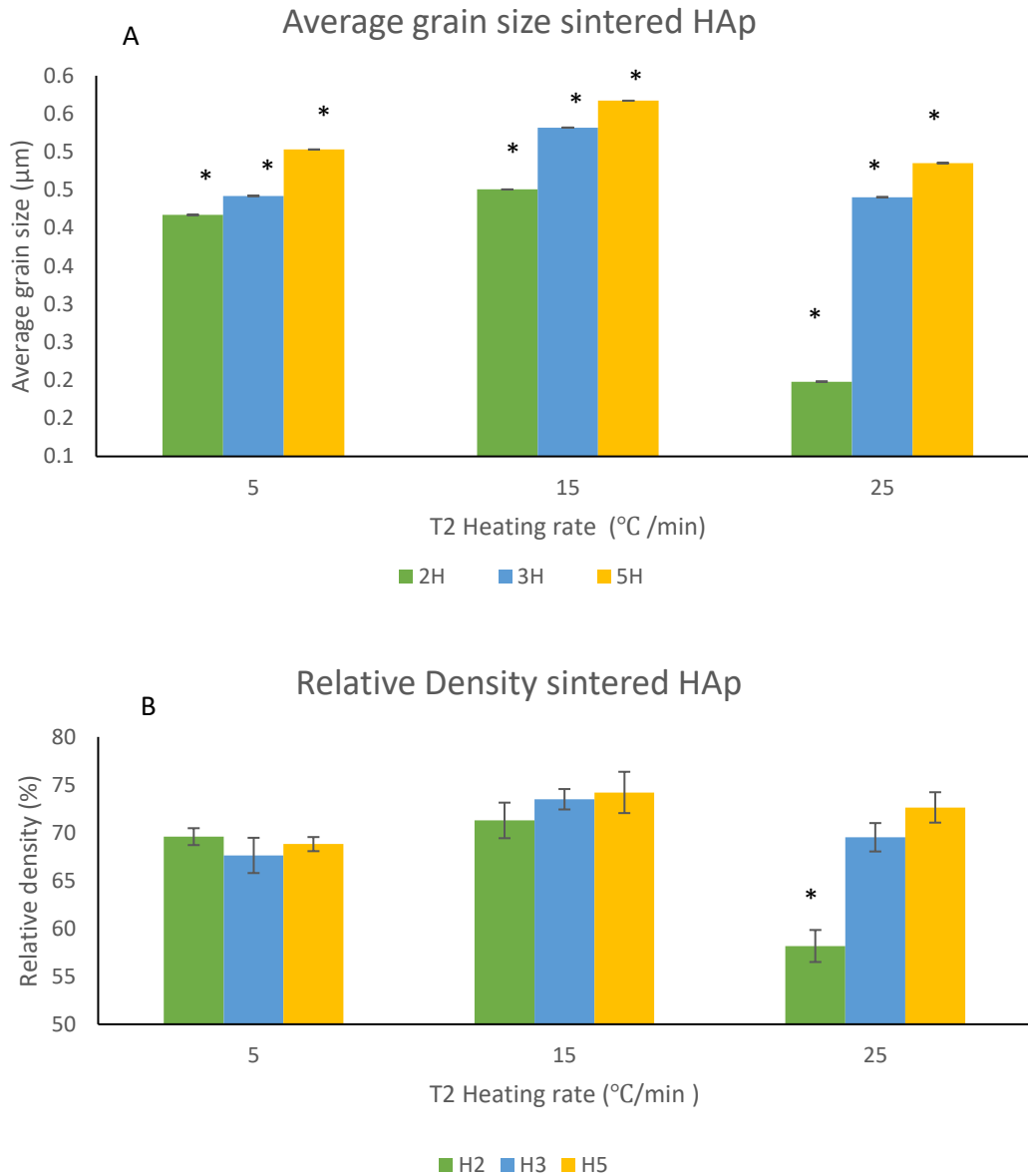


Figure 32. (A) Average grain size and (B) Relative density results of DOE of sintered structures. The asterisk represents a significant difference from the group at ($p < 0.05$)

Additionally, it was found that uniform densification through HAp samples was a function of its thickness when thick (more than ~1.2mm) HAp samples were sintered. Detailed inspection revealed that non-uniform densification was obtained. The external surfaces of the bulk material had a microstructure comparable to the final stage of sintering with almost no porosity (figure 4.15

A and B) while the interior had a microstructure similar to the intermediate stage of sintering with more porosity and necking of the grains (figure 4.15 D). This can be seen in figure 4.15.

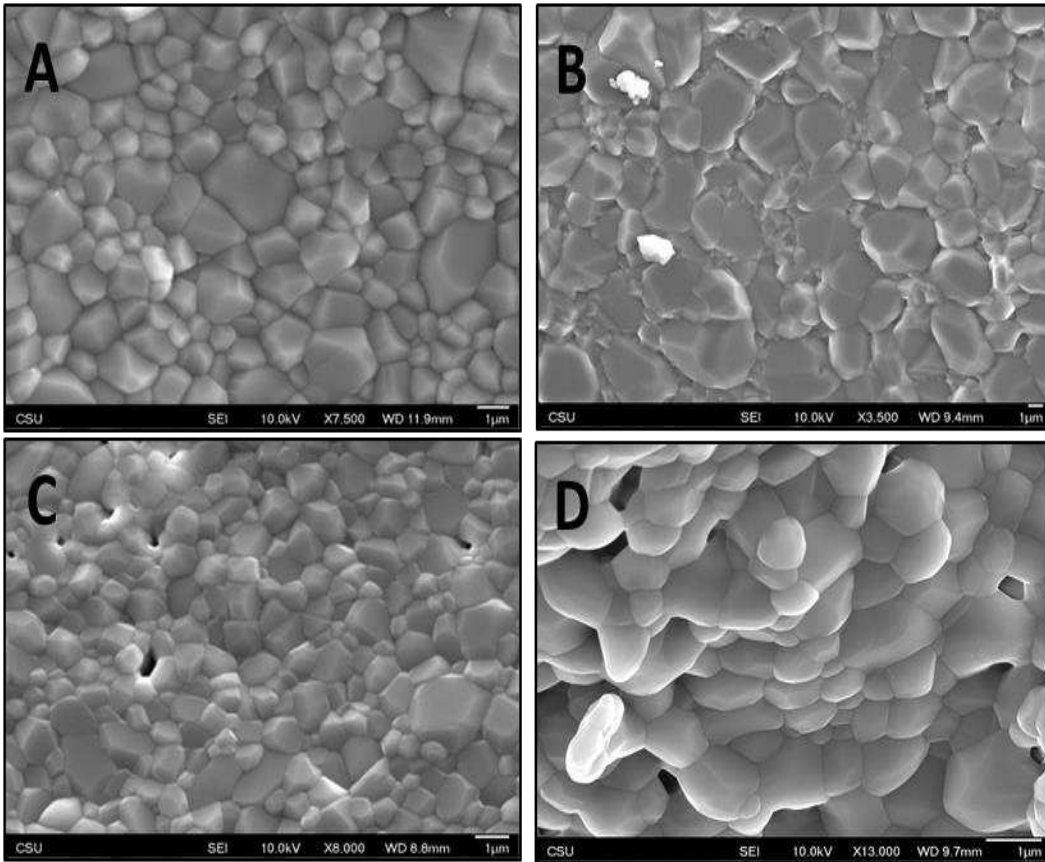


Figure 33 Different densification presented in HAp sintered structures. (A) top surface; (B) bottom surface; (C)lateral surface and (D) interior of HAp sintered structure.

The non-uniformity in the densification of the samples could be the result of a temperature gradient between the interior and exterior of the sample. Conduction of heat from the hot air into the bulk material would be limited by the thermal resistance of the material. The surfaces that were in direct contact with the hot air surrounding the material experienced a higher temperature that enabled densification. In the interior, the temperature could have been lower due to the thermal resistance of HAp. Therefore, there would be a less driving force for densification in the interior compared to the surface.

Shrinkage of the HAp samples was also measured. Figure 4.16 presents a sample before and after sintering. It was apparent that uniform shrinkage occurred in all directions for symmetric samples. For cubic samples, the shrinkage in each dimension was $15.92\pm 0.95\%$.

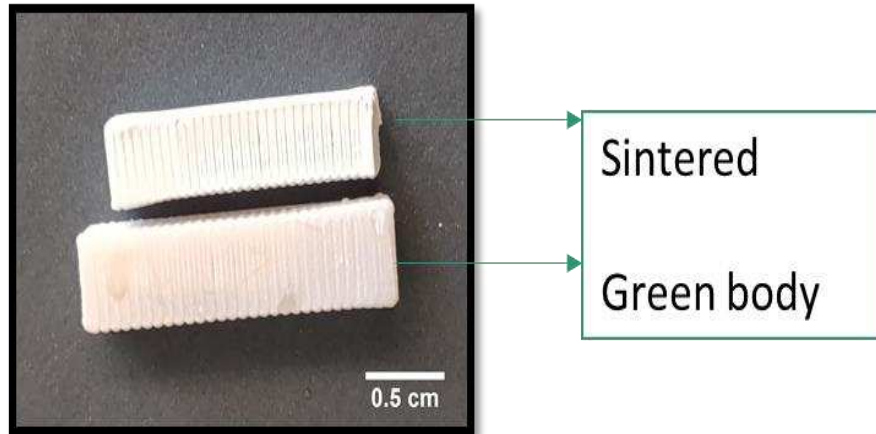


Figure 34. Shrinkage of HAp samples. The top sample corresponds to a sintered structure that had the same dimensions as the bottom sample (HAp/PEGDMA green body) before sintering.

4.5. Flexural Strength

Characteristic stress vs. strain curves obtained from the four-point bending test of the green bodies and sintered HAp samples are presented in figure 4.17. In general, both materials had a brittle nature and failed before presenting any plastic deformation.

For the green bodies, upon irradiation, the EGDMA covalently bonded into a highly crosslinked and interconnected network reinforced with the HAp particles. This formed a stiff material. Moreover, the lack of plastic deformation may be explained by the short length of polymer chains present in the sample connected very tightly.

For the sintered samples, the known brittle nature of HAp was verified by the bend testing performed here. Moreover, the flexural strength could be affected by the $\sim 27\%$ undesired porosity obtained from the sintering process leading to a low flexural strength and modulus.

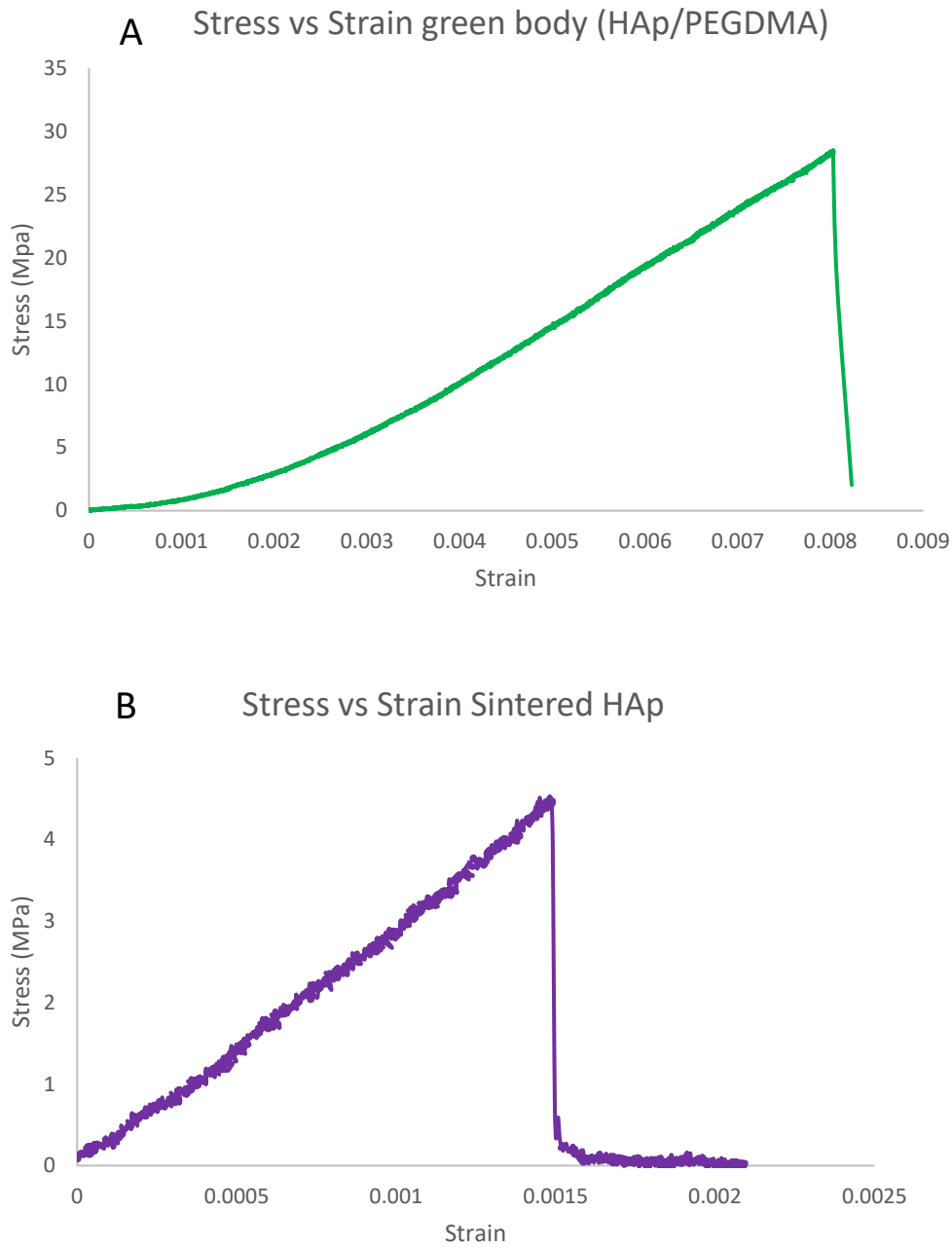


Figure 35. Characteristic flexural Stress vs. Strain curves obtained in 4-point bending for (A) HAp/PEGDMA green bodies and (B) HAp sintered structures.

Flexural modulus and strength of the green bodies were higher than the values obtained for the sintered samples. These are reported in table 7 and figure 4.18. Sintered samples without visible

flaws were not possible to produce. Crack formation in the sintering process could not be avoided. Possible, the temperature gradient producing non-uniform densification in the samples had bigger effects in large samples producing localize stresses until these led to crack formations. Therefore, all flexural tests for sintered samples had to be performed with samples containing pre-existing cracks.

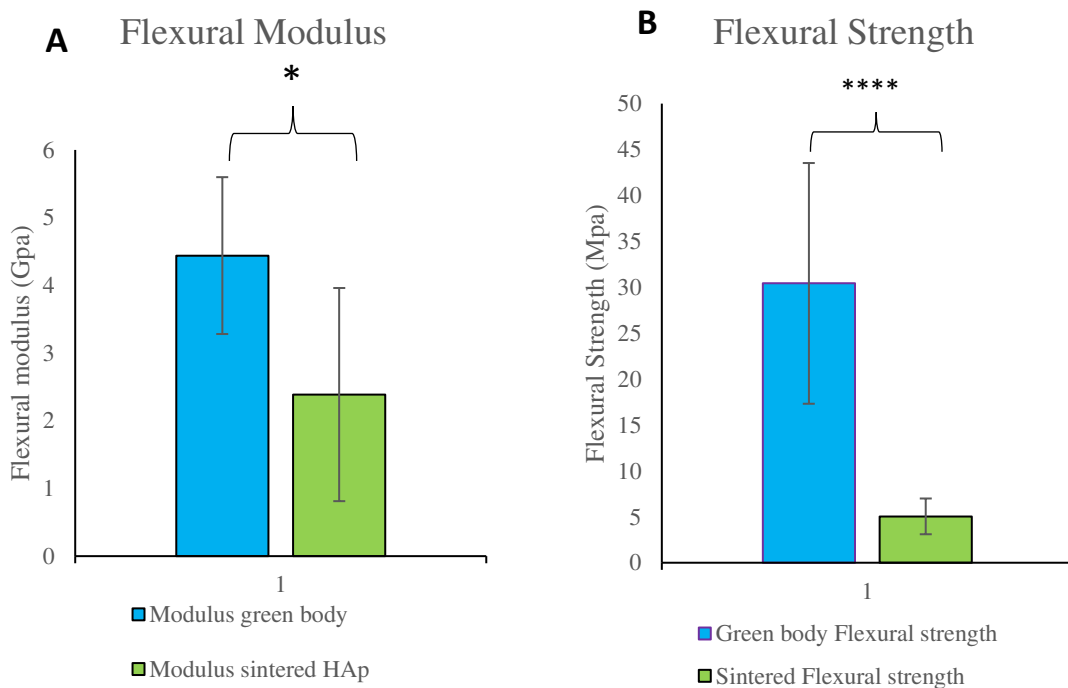


Figure 36. Flexural Modulus and flexural strength of HAp/PEGDMA and sintered HAp structures

Flexural strength of green bodies appeared to be compatible with trabecular bone. Green bodies had superior mechanical properties because PEGDMA behaves like an adhesive and crack stopper. The PEGDMA bound the HAp particles together, thereby opposing crack growth.

In the case of sintered HAp, the samples contain β -TCP as XRD confirmed, and it is known that TCPs have lower mechanical strength than HAp [18]. Thus, β -TCP in the HAp sintered samples

in addition to pre-existing cracks, brittle nature, non-uniform densification, and ~27% porosity, decreased its mechanical strength.

Table 7. Flexural properties of green and sintered bodies. Value in the red box is similar to trabecular bone.

Flexural	Green body	Sintered HAp	Cortical Bone [11]	Trabecular Bone [11]
Strength (S) (MPa)	30.42±13.11	5.05±1.94	135-193	10-20
Modulus (GPa)	4.44±1.16	2.39±1.57	10-20	0.1-5

Bose et al. created a table comparing different materials that were developed to produce 3D printed scaffolds for orthopedic applications [34]. This is shown in table 8. Comparing the bending properties of PEGDMA/HAp green bodies to other scaffolds, the green bodies of this study presented the third highest flexural strength and the second highest modulus.

Table 8. Mechanical properties of scaffolds created by other authors and the results of this research are shown in green. Table modified from [34]

Material	Bending Modulus (GPa)	Bending Strength (MPa)	Reference
Human cortical bone	-	135-193	[11]
Human Trabecular bone	-	2-12	[11]
HAp/A-W glass	0.35	1.27	[55]
HAp/A-W glass-sintered at 1300°C	34.1	76.82	[55]
HAp	0.4	0.69	[56]
HAp/bis-GMA	6.2	50	[56]
PEGDMA/HAp	4.44±1.16	30.42±13.11	Lopez-Ambrosio
Sintered HAp	2.39±1.57	5.05± 1.94	Lopez-Ambrosio

After flexural testing, the fracture surfaces were analyzed. In figure 4.19, SEM images of the fracture surface of the green bodies are presented. In figure 4.19.A. the origin of the fracture (O)

is located near the surface edge. Moreover, it was possible to identify the fracture mirror (M), mist hackles (MH) and hackles (H). Figure 4.19.B and C show a closer view of the hackle lines, and figure 4.19.D shows brittle fracture in agreement with the stress versus strains curves with no signs of plastic deformation.

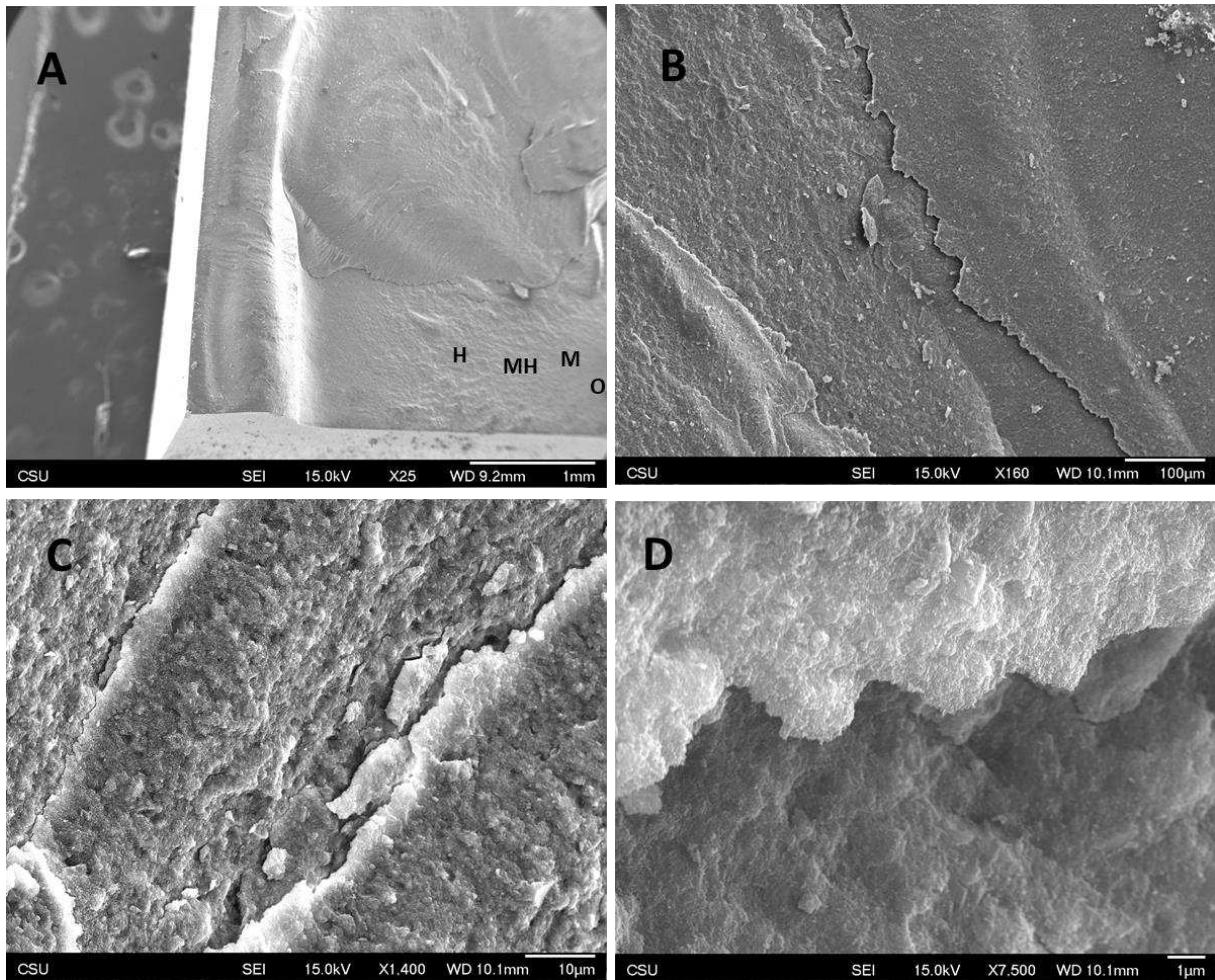


Figure 37. Fracture surface of green bodies. (A) 25x magnification: fracture origin can be seen O: origin, M: mirror fracture, MH: mist hackle, H: hackle. (B) 150x magnification: fracture produced by the mirror pattern. (C) 1400x magnification: fracture from mirror pattern closer view (D) brittle fracture.

Micrographs of the bending fracture surfaces of the sintered HAp are shown in figure 4.20. As was explained before, samples with pre-existing cracks inherent from the sintering process were tested.

The pre-existing cracks can be seen in figure 4.20.A.

From the fracture surfaces, it was not possible to identify the origin from which the sample failed. The reason could be that many of the pre-existing cracks contributed to the final failure fracture redistributing the stress in various locations of the sample.

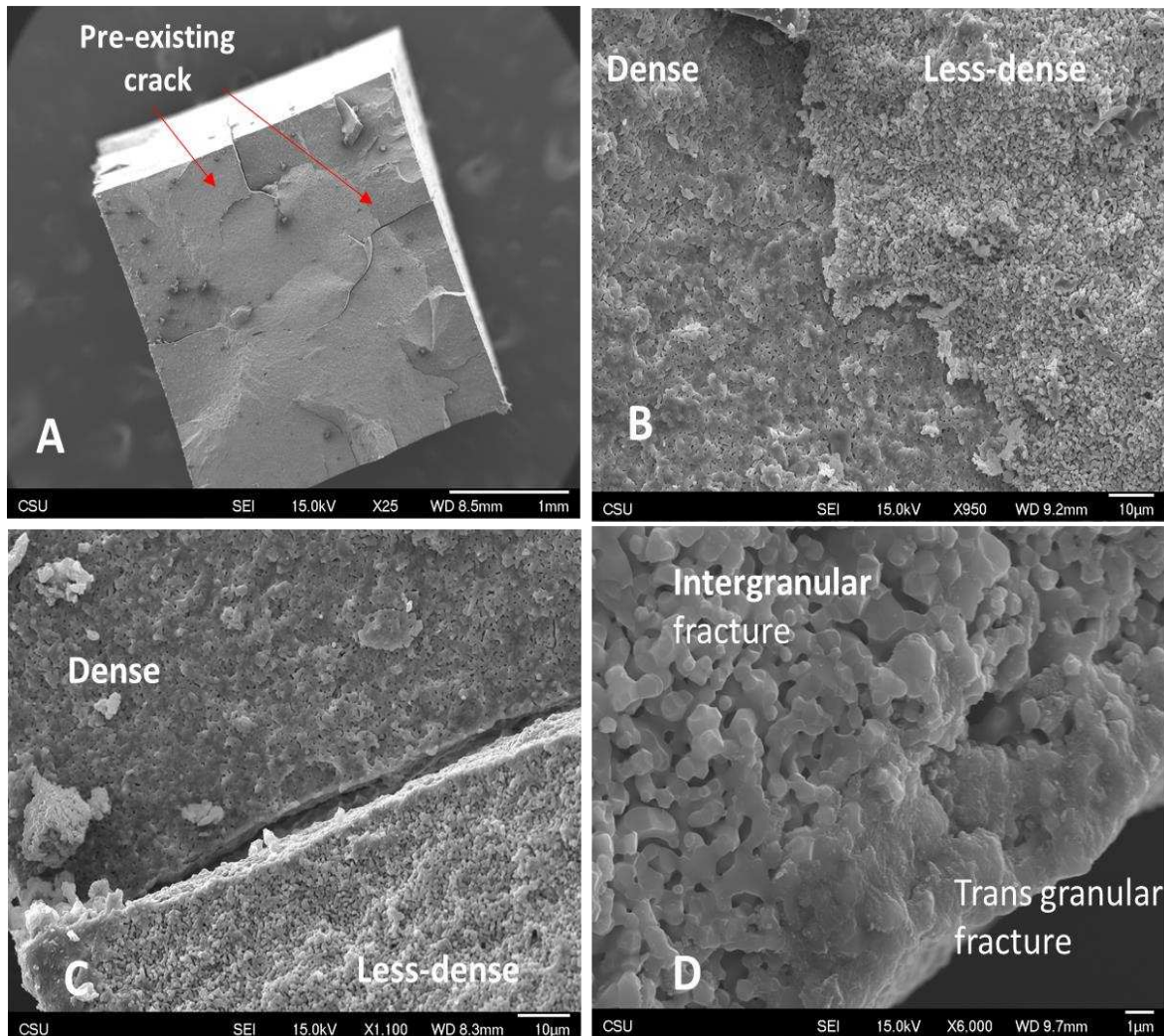


Figure 38. Fracture surface sintered HAp. (A) 25x magnification: evidence of pre-existing cracks. (B) and (C) 950x and 1100x magnification show two types of densification. (D) 6000x magnification: intergranular fracture in less-dense zones and trans granular fracture in denser zones of the sample.

Moreover, two types of HAp grain densification could be observed in the surfaces (figure 4.20.b, c). In the denser areas, the fracture propagation mechanism corresponded to trans-granular while in the porous areas, the mechanism was intergranular. Different densification in the interior of the

samples could be explained by understanding the schematic 4.21. Pre-existing fractures created gaps that permitted the penetration of hot air, as discussed in Section 4.4. Thus, the sides of the fractures and outer surfaces had the same temperature of the set point. This enabled better densification of the samples in these regions. In contrast, the interior areas that were not close to pre-existing cracks or outer surfaces had a lower sintering temperature due to the thermal resistance of HAp. This hindered the extent of sintering in the sample interiors which became exposed after flexural testing.

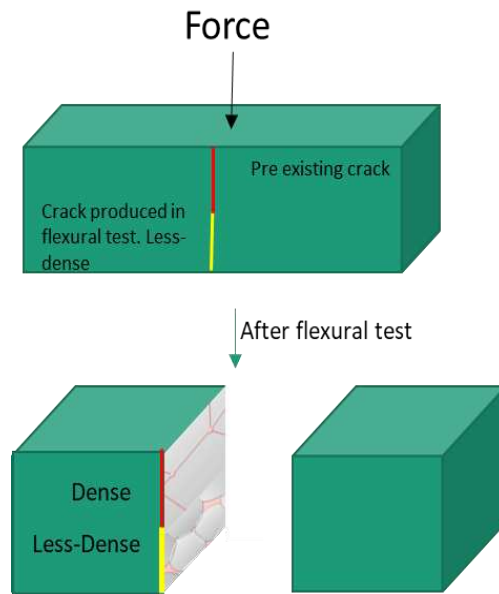


Figure 39. Schematic explaining cause for different densification. Red line represents pre-existing crack and yellow line represents crack created after the flexural test.

4.6. Cytotoxicity Studies in sintered HAp samples

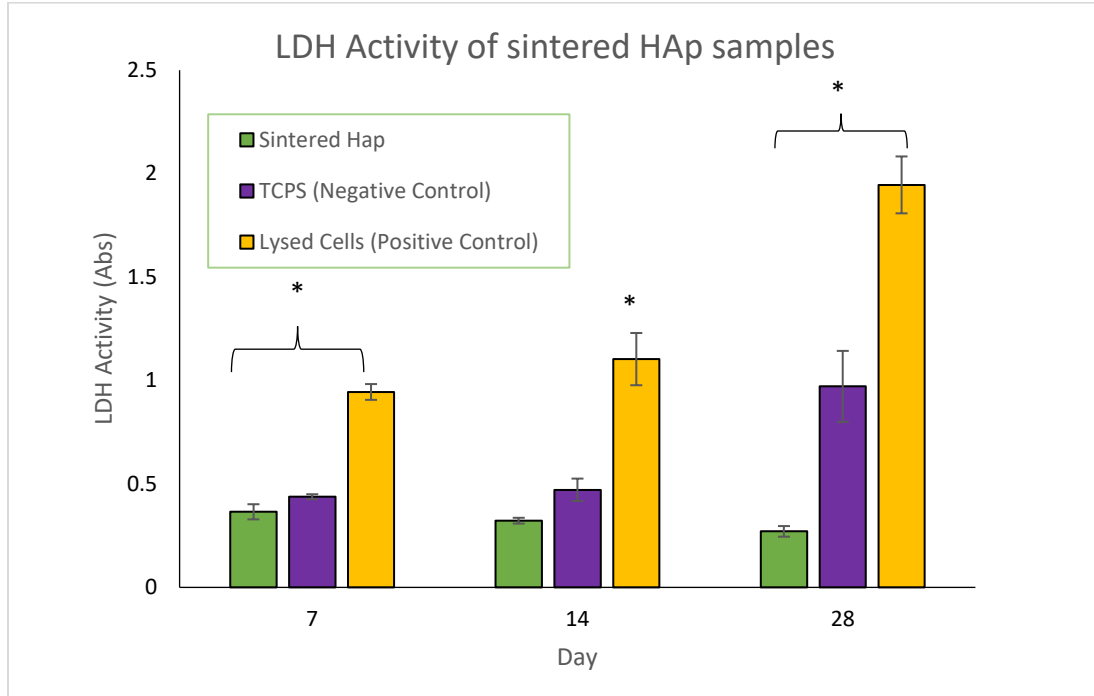


Figure 40. LDH Activity of sintered HAp samples for day 7, 14 and 28.

LDH levels obtained from the cytotoxicity study are reported in figure 4.22. After letting the extracts of the HAp samples leach into the media for three different periods, the ADSCs cells were incubated for 24h. Then, the LDH levels were measured.

For the three different periods corresponding to 7, 14, and 28 days, the HAp samples presented the lowest LDH activity compared to the positive and negative controls, significantly lower than negative controls ($p \leq 0.05$) at all times. Low LDH activity proved that HAp samples were not cytotoxic to ADSCs.

5. CONCLUSIONS

The following section presents the conclusions from the results obtained above.

Pretreatment of HAp from two different vendors using ball milling and heat treatment to change morphology was achieved. However, pretreated HAp powders were not stable in EGDMA for all cases studied in this project.

HAp photopolymerizable resins with a high volume of Macron as received HAp particles were successfully produced in 8h using a planetary ball mill with agate milling balls. It was determined that HAp resins were homogenous.

Storage conditions of HAp slurries effectively prevented exposure to light, possible photopolymerization reaction, and evaporation of EDGMA, but they should be kept in storage for less than 20 days to avoid an increase in viscosity.

Shear thinning behavior of HAp slurries enabled the control of flow deposition in the fabrication of complex parts by a 3D printing process that combined viscous extrusion and photopolymerization. It was possible to build complex structures that had complete layer cohesion with no support material.

Scaffolds with different pores sizes from $\sim 130 \mu\text{m}$ were 3D printed using 41 vol% HAp slurries. Visual inspection, SEM, and fluid flow verified that the pores were interconnected through the structures, leading to the belief that these scaffolds could be used for cell growth in orthopedic applications, decreasing the risk posed by poor perfusion during fracture healing.

$\sim 78\%$ relative density was obtained for thin HAp samples in a two-step sintering process. For thicker samples, densification was dependent on its thickness. Flaws and non-uniform densification were unavoidable for samples thicker than 1.2mm.

Flexural strength of PEGDMA-HAp samples (Green bodies) were higher than HAp sintered samples. PEGDMA-HAp samples presented flexural strength similar to trabecular bone.

Sintered HAp structures were not cytotoxic for ADSCs cells. Green bodies were not tested because at having some content of photoinitiator; the samples were considered toxic.

This technique and material with further development has the potential to be used to produce custom bone implants.

6. SUMMARY OF WORK AND FUTURE DIRECTIONS

Change in the morphology of Mk Nano and Macron HAp powders were achieved by a ball milling and heat treatment, respectively. However, these efforts were not enough to find suitable morphology, size, and specific surface area of the particles that maintained them disperse and decreased the viscosity in HAp slurries. On one hand, Mk Nano HAp was reduced to a particle smaller than 100nm producing an extensive specific surface area and a loss of the spherical shape. On the other hand, Macron HAp primitive needle-like particles agglomerated in semi-spherical clusters that after the heat treatment, coalesced into porous particles. This increased the overall Macron HAp particle size but did not decrease the specific surface area. Therefore, Macron HAp as-received, had to be used in the production of the HAp 41 vol% slurries.

Using as-received Macron HAp with a specific surface area of $67\text{m}^2/\text{g}$, the amount of dispersant D540 needed to stabilize the colloid (HAp-EGDMA) was very large (\sim six wt%) to cover sufficiently the surface area and maintain stability in the dispersion. Thus, the strong shear thinning behavior and high viscosity of the slurry was a product of the morphology and specific surface area of the as-received Macron HAp, in addition to a large amount of dispersant and the high solid loading of HAp particles. Therefore, more efforts should be directed to address the synthesis and control of HAp particles to obtain a lower specific surface area while still maintaining spherical shape. If this can be achieved, several advancements may be made. For instance, the overall viscosity of the slurry may decrease, allowing for easier mixing and shorter processing times. Another advancement may be an increase in the volume percent of HAp that may be stabilized in the slurry.

Using a planetary ball mill, the production time of 41vol% HAp slurries was decreased to 8h, and homogenous slurries were produced. This method is effective to mix a high load of HAp particles

and disperse them in EGDMA. Viscous extrusion and layer-wise photo-curing were used to 3D print complex HAp structures and opened the possibility of printing other high viscosity slurries. However, more studies should address the curing mechanics of the photopolymer as a function of the exposed top view cross-sectional area. The curing of each road is a function of the light intensity and exposure time. For instance, a square with no infill will require less exposure time than the same square with 100% infill. Thus, for the square with 100% infill, far less intensity of light will be required to cure the part. This study was limited to a trial and error approach to determine the proper intensity of light for the part with different shapes and infills. If a part was over cured, differentiation between the layers due to rapid photopolymerization (hardening in the road), and cracking due to thermal expansion was noticeable. If a part was under cured, distortion in the structure was visible. Thus, it will be ideal for developing a relationship between exposure time and light intensity that could be used without a dependency on the geometry of the part or infill.

Moreover, more development in the liquid photopolymerizable phase is critical. When EGDMA is in the liquid phase, the density of the bifunctional groups is very high. Thus, when the photopolymer is initiated by light, multiple exothermic reactions begin increasing the temperature and producing shrinkage of the polymer due to the consumption of the double C-C bond of the parts. These lead to undesirable defects that increase with the size of the parts or/and its percent infill. As an example, warping and cracks were found in the densest parts. Therefore, a combination of light-sensitive monomers or dilution of EGDMA may decrease shrinkage and prevent the rise in temperature in the printed structures.

Sintering as a method to consolidate HAp particles and pyrolyze the polymer matrix produced with up to ~78% relative density in thin samples. However, efforts to find better results in the

sintering process that eliminates residual porosity are important because scaffolds with design and residual porosity (see figure 6.1) are weaker than scaffolds with only design porosity. Moreover, uniform densification was a function of the thickness of the sample and was a result of thermal gradients in the sintering. Non-uniform distribution of densification produced localized stresses that caused cracks in the parts. Future work determining a relationship between part size and sintering holding time (T1) should be addressed to obtain uniform densification and minimize cracking. The issue above, in addition to the brittle nature of HAp, showed less flexural strength than their green bodies. Thus, mechanisms for avoiding thermal gradients in the sintering process and strengthening mechanisms of HAp should be investigated.

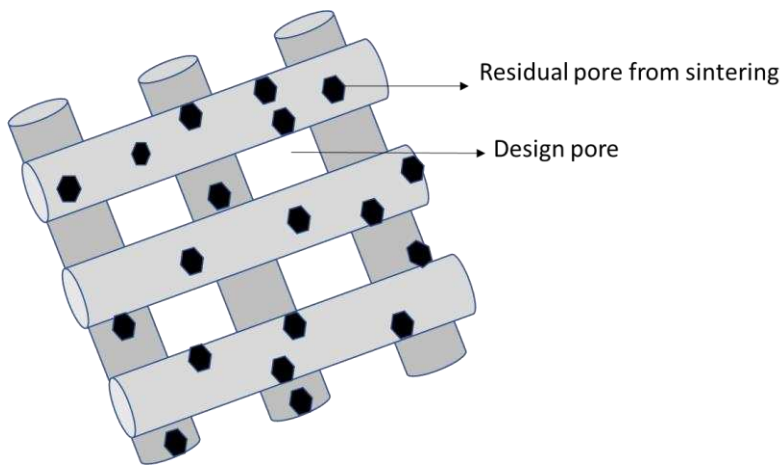


Figure 41. Sintered scaffold with residual and design porosity

Green bodies showed higher flexural strength than HAp sintered bodies, so cytotoxicity studies should be addressed to find the cytotoxic behavior of the PEGDMA-HAp. If PEGDMA-HAp can be formulated to be non-cytotoxic, this may open the possibility of using the material for biomedical applications.

REFERENCES

- [1] G.M. Calori, W. Albisetti, A. Agus, S. Iori, L. Tagliabue, Risk factors contributing to fracture non-unions, *Injury*. 38 (2007) S11–S18. doi:10.1016/S0020-1383(07)80004-0.
- [2] G.M. Calori, E. Mazza, M. Colombo, C. Ripamonti, The use of bone-graft substitutes in large bone defects: Any specific needs?, *Injury*. 42 (2011) S56–S63. doi:10.1016/j.injury.2011.06.011.
- [3] J.B. Park, J.D. Bronzino, eds., *Biomaterials: principles and applications*, CRC Press, Boca Raton, 2002.
- [4] W. Wang, K.W.K. Yeung, Bone grafts and biomaterials substitutes for bone defect repair: A review, *Bioact. Mater.* 2 (2017) 224–247. doi:10.1016/j.bioactmat.2017.05.007.
- [5] W.R. Walsh, R.A. Oliver, C. Christou, V. Lovric, E.R. Walsh, G.R. Prado, T. Haider, Critical Size Bone Defect Healing Using Collagen–Calcium Phosphate Bone Graft Materials, *PLOS ONE*. 12 (2017) e0168883. doi:10.1371/journal.pone.0168883.
- [6] C.A. Lee, T.A. Einhorn, Chapter 1 - The Bone Organ System: Form and Function, in: R. Marcus, D. Feldman, J. Kelsey (Eds.), *Osteoporosis*. Second Ed., Academic Press, San Diego, 2001: pp. 3–20. doi:10.1016/B978-012470862-4/50002-7.
- [7] I.H. Kalfas, Principles of bone healing, *Neurosurg. Focus*. 10 (2001) 1–4. doi:10.3171/foc.2001.10.4.2.
- [8] G.C. Wang, Z.F. Lu, H. Zreiqat, 8 - Bioceramics for skeletal bone regeneration, in: K. Mallick (Ed.), *Bone Substit. Biomater.*, Woodhead Publishing, 2014: pp. 180–216. doi:10.1533/9780857099037.2.180.
- [9] E.F. Morgan, G.L. Barnes, T.A. Einhorn, Chapter 1 - The Bone Organ System: Form and Function, in: R. Marcus, D. Feldman, D.W. Dempster, M. Luckey, J.A. Cauley (Eds.), *Osteoporosis*. Fourth Ed., Academic Press, San Diego, 2013: pp. 3–20. doi:10.1016/B978-0-12-415853-5.00001-7.
- [10] M. Doblaré, J.M. García, M.J. Gómez, Modelling bone tissue fracture and healing: a review, *Eng. Fract. Mech.* 71 (2004) 1809–1840. doi:10.1016/j.engfracmech.2003.08.003.
- [11] Q. Fu, E. Saiz, M.N. Rahaman, A.P. Tomsia, Bioactive glass scaffolds for bone tissue engineering: state of the art and future perspectives, *Mater. Sci. Eng. C*. 31 (2011) 1245–1256. doi:10.1016/j.msec.2011.04.022.
- [12] P.V. Giannoudis, T.A. Einhorn, D. Marsh, Fracture healing: The diamond concept, *Injury*. 38 (2007) S3–S6. doi:10.1016/S0020-1383(08)70003-2.
- [13] E.A. Calmar, R.J. Vinci, The anatomy and physiology of bone fracture and healing, *Clin. Pediatr. Emerg. Med.* 3 (2002) 85–93. doi:10.1053/epem.2002.127037.
- [14] S.R. Dutta, D. Passi, P. Singh, A. Bhuibhar, Ceramic and non-ceramic hydroxyapatite as a bone graft material: a brief review, *Ir. J. Med. Sci.* 1971 -. 184 (2015) 101–106. doi:10.1007/s11845-014-1199-8.
- [15] K. Li, C.Y. Yeung, K.W.K. Yeung, S.C. Tjong, Sintered Hydroxyapatite/Polyetheretherketone Nanocomposites: Mechanical Behavior and Biocompatibility, *Adv. Eng. Mater.* 14 (2012) B155–B165. doi:10.1002/adem.201080145.
- [16] Z. Zhou, D. Yang, J. Nie, Y. Ren, F. Cui, Injectable Poly(ethylene glycol) Dimethacrylate-based Hydrogels with Hydroxyapatite, *J. Bioact. Compat. Polym.* 24 (2009) 405–423. doi:10.1177/0883911509341774.

- [17] J.-L. Liu, Y.-Y. Zhu, Q.-L. Wang, S.-R. Ge, Biotribological behavior of ultra high molecular weight polyethylene composites containing bovine bone hydroxyapatite, *J. China Univ. Min. Technol.* 18 (2008) 606–612.
- [18] A. Haider, S. Haider, S.S. Han, I.-K. Kang, Recent advances in the synthesis, functionalization and biomedical applications of hydroxyapatite: a review, *RSC Adv.* 7 (2017) 7442–7458. doi:10.1039/C6RA26124H.
- [19] E. Andrzejewska, Chapter 2 - Free Radical Photopolymerization of Multifunctional Monomers, (n.d.) 20.
- [20] S.C. Ligon, R. Liska, J. Stampfl, M. Gurr, R. Mülhaupt, Polymers for 3D Printing and Customized Additive Manufacturing, *Chem. Rev.* 117 (2017) 10212–10290. doi:10.1021/acs.chemrev.7b00074.
- [21] E. Andrzejewska, Photopolymerization kinetics of multifunctional monomers, *Prog. Polym. Sci.* 26 (2001) 605–665. doi:10.1016/S0079-6700(01)00004-1.
- [22] J.-P. Fouassier, J. Lalev?e, Photoinitiators for Polymer Synthesis: Scope, Reactivity, and Efficiency, John Wiley & Sons, 2012.
- [23] I. Gibson, D.W. Rosen, B. Stucker, Additive manufacturing technologies: rapid prototyping to direct digital manufacturing, Springer, London ; New York, 2010.
- [24] J.W. Halloran, Ceramic Stereolithography: Additive Manufacturing for Ceramics by Photopolymerization, *Annu. Rev. Mater. Res.* 46 (2016) 19–40. doi:10.1146/annurev-matsci-070115-031841.
- [25] E.R. Leite, C. Ribeiro, Basic Principles: Thermodynamics and Colloidal Chemistry, in: *Cryst. Growth Colloidal Nanocrystals*, Springer New York, New York, NY, 2012: pp. 7–17. doi:10.1007/978-1-4614-1308-0_2.
- [26] K. Holmberg, D.O. Shah, M.J. Schwuger, eds., *Handbook of applied surface and colloid chemistry*, Wiley, Chichester, England ; New York, 2002.
- [27] T.F. Tadros, ed., *Colloid stability: the role of surface forces*, Wiley-VCH Verlag, Weinheim, 2007.
- [28] J.A. Lewis, Colloidal Processing of Ceramics, *J. Am. Ceram. Soc.* 83 (2004) 2341–2359. doi:10.1111/j.1151-2916.2000.tb01560.x.
- [29] R. Trombetta, J.A. Inzana, E.M. Schwarz, S.L. Kates, H.A. Awad, 3D Printing of Calcium Phosphate Ceramics for Bone Tissue Engineering and Drug Delivery, *Ann. Biomed. Eng.* 45 (2017) 23–44. doi:10.1007/s10439-016-1678-3.
- [30] M. Faes, H. Valkenaers, F. Vogeler, J. Vleugels, E. Ferraris, Extrusion-based 3D Printing of Ceramic Components, *Procedia CIRP.* 28 (2015) 76–81. doi:10.1016/j.procir.2015.04.028.
- [31] S.-I. Roohani-Esfahani, P. Newman, H. Zreiqat, Design and Fabrication of 3D printed Scaffolds with a Mechanical Strength Comparable to Cortical Bone to Repair Large Bone Defects, *Nature.* 6 (2016). doi:10.1038/srep19468.
- [32] M. Castilho, C. Moseke, A. Ewald, U. Gbureck, J. Groll, I. Pires, J. Te's smar, E. Vorndran, Direct 3D powder printing of biphasic calcium phosphate scaffolds for substitution of complex bone defects, *Biofabrication.* 6 (2014) 015006.
- [33] S. Bose, A. Banerjee, S. Dasgupta, A. Bandyopadhyay, Synthesis, Processing, Mechanical, and Biological Property Characterization of Hydroxyapatite Whisker-Reinforced Hydroxyapatite Composites, *J. Am. Ceram. Soc.* 92 (2009) 323–330. doi:10.1111/j.1551-2916.2008.02881.x.

- [34] S. Bose, S. Vahabzadeh, A. Bandyopadhyay, Bone tissue engineering using 3D printing, *Mater. Today*. 16 (2013) 496–504. doi:10.1016/j.mattod.2013.11.017.
- [35] B. Duan, M. Wang, W.Y. Zhou, W.L. Cheung, Z.Y. Li, W.W. Lu, Three-dimensional nanocomposite scaffolds fabricated via selective laser sintering for bone tissue engineering, *Acta Biomater.* 6 (2010) 4495–4505. doi:10.1016/j.actbio.2010.06.024.
- [36] S.K. Nandi, G. Fielding, D. Banerjee, A. Bandyopadhyay, S. Bose, 3D-printed β -TCP bone tissue engineering scaffolds: Effects of chemistry on in vivo biological properties in a rabbit tibia model, *J. Mater. Res.* 33 (2018) 1939–1947. doi:10.1557/jmr.2018.233.
- [37] G. Gao, A.F. Schilling, T. Yonezawa, J. Wang, G. Dai, X. Cui, Bioactive nanoparticles stimulate bone tissue formation in bioprinted three-dimensional scaffold and human mesenchymal stem cells, *Biotechnol. J.* 9 (2014) 1304–1311. doi:10.1002/biot.201400305.
- [38] A.E. Jakus, A.L. Rutz, S.W. Jordan, A. Kannan, S.M. Mitchell, C. Yun, K.D. Koube, S.C. Yoo, H.E. Whiteley, C.-P. Richter, R.D. Galiano, W.K. Hsu, S.R. Stock, E.L. Hsu, R.N. Shah, Hyperelastic “bone”: A highly versatile, growth factor–free, osteoregenerative, scalable, and surgically friendly biomaterial, *Sci. Transl. Med.* 8 (2016) 358ra127–358ra127. doi:10.1126/scitranslmed.aaf7704.
- [39] R. Alluri, A. Jakus, S. Bougioukli, W. Pannell, O. Sugiyama, A. Tang, R. Shah, J.R. Lieberman, 3D printed hyperelastic “bone” scaffolds and regional gene therapy: A novel approach to bone healing: 3D printed hyperelastic “bone” scaffolds, *J. Biomed. Mater. Res. A.* 106 (2018) 1104–1110. doi:10.1002/jbm.a.36310.
- [40] C. Koski, B. Onuiké, A. Bandyopadhyay, S. Bose, Starch-hydroxyapatite composite bone scaffold fabrication utilizing a slurry extrusion-based solid freeform fabricator, *Addit. Manuf.* 24 (2018) 47–59. doi:10.1016/j.addma.2018.08.030.
- [41] M. Asif, J.H. Lee, M.J. Lin-Yip, S. Chiang, A. Levaslot, T. Giffney, M. Ramezani, K.C. Aw, A new photopolymer extrusion 5-axis 3D printer, *Addit. Manuf.* 23 (2018) 355–361. doi:10.1016/j.addma.2018.08.026.
- [42] R.D. Farahani, L.L. Lebel, D. Therriault, Processing parameters investigation for the fabrication of self-supported and freeform polymeric microstructures using ultraviolet-assisted three-dimensional printing, *J. Micromechanics Microengineering.* 24 (2014) 055020. doi:10.1088/0960-1317/24/5/055020.
- [43] R.H.R. Castro, K. van Benthem, eds., *Sintering: mechanisms of convention nanodensification and field assisted processes*, Springer, Berlin ; New York, 2013.
- [44] M. Prakasam, J. Locs, K. Salma-Ancane, D. Loca, A. Largeteau, L. Berzina-Cimdina, *Fabrication, Properties and Applications of Dense Hydroxyapatite: A Review*, *J. Funct. Biomater.* 6 (2015) 1099–1140. doi:10.3390/jfb6041099.
- [45] K. Ikemura, K. Ichizawa, M. Yoshida, S. Ito, T. Endo, UV-VIS spectra and photoinitiation behaviors of acylphosphine oxide and bisacylphosphine oxide derivatives in unfilled, light-cured dental resins, *Dent. Mater. J.* 27 (2008) 765–774. doi:10.4012/dmj.27.765.
- [46] European Commission, Directorate General for Health & Consumers, Trimethylbenzoyl diphenylphosphine oxide (TPO)., European Commission, Luxembourg, 2014. <http://dx.publications.europa.eu/10.2772/45370> (accessed March 3, 2019).
- [47] H.K. Park, M. Shin, B. Kim, J.W. Park, H. Lee, A visible light-curable yet visible wavelength-transparent resin for stereolithography 3D printing, *NPG Asia Mater.* 10 (2018) 82. doi:10.1038/s41427-018-0021-x.
- [48] M.A. Janney, Attaining high solids in ceramic slurries, Webpage [www.Ornl.gov/MC-SPGgelpubs/Mixing/Pdf/Oakridge Natl. Lab. Oakridge TN.](http://www.Ornl.gov/MC-SPGgelpubs/Mixing/Pdf/Oakridge%20Natl.%20Lab.%20Oakridge%20TN.%20(2001).) (2001).

- [49] T.G. Aguirre, C.L. Cramer, V.P. Torres, T.J. Hammann, T.B. Holland, K. Ma, Effects of the addition of boron nitride nanoplate on the fracture toughness, flexural strength, and Weibull Distribution of hydroxyapatite composites prepared by spark plasma sintering, *J. Mech. Behav. Biomed. Mater.* 93 (2019) 105–117. doi:10.1016/j.jmbbm.2019.01.021.
- [50] R. Dorey, Chapter 2 - Routes to thick films: What is a thick film? How is it made?, in: *Ceram. Thick Films MEMS Microdevices*, William Andrew Publishing, Oxford, 2012: pp. 35–61. doi:10.1016/B978-1-4377-7817-5.00002-X.
- [51] L.W. McKeen, 5 - Pigments, Fillers, and Extenders, in: *Fluorinated Coat. Finish. Handb.*, William Andrew Publishing, Norwich, NY, 2006: pp. 59–76. doi:10.1016/B978-081551522-7.50008-X.
- [52] R.P. Chhabra, Non-Newtonian Fluids: An Introduction, in: J.M. Krishnan, A.P. Deshpande, P.B.S. Kumar (Eds.), *Rheol. Complex Fluids*, Springer New York, New York, NY, 2010: pp. 3–34. doi:10.1007/978-1-4419-6494-6_1.
- [53] S.J. Kalita, S. Bose, H.L. Hosick, A. Bandyopadhyay, Development of controlled porosity polymer-ceramic composite scaffolds via fused deposition modeling, *Mater. Sci. Eng. C.* 23 (2003) 611–620. doi:10.1016/S0928-4931(03)00052-3.
- [54] N.J. Lóh, L. Simão, C.A. Faller, A. De Noni, O.R.K. Montedo, A review of two-step sintering for ceramics, *Ceram. Int.* 42 (2016) 12556–12572. doi:10.1016/j.ceramint.2016.05.065.
- [55] J. Suwanprateeb, R. Sanngam, W. Suvannapruk, T. Panyathanmaporn, Mechanical and in vitro performance of apatite–wollastonite glass ceramic reinforced hydroxyapatite composite fabricated by 3D-printing, *J. Mater. Sci. Mater. Med.* 20 (2009) 1281–1289. doi:10.1007/s10856-009-3697-1.
- [56] J. Suwanprateeb, R. Sanngam, W. Suwanpreuk, Fabrication of bioactive hydroxyapatite/bis-GMA based composite via three dimensional printing, *J. Mater. Sci. Mater. Med.* 19 (2008) 2637–2645. doi:10.1007/s10856-007-3362-5.

APPENDIX 1: 41% Vol hydroxyapatite slurry mixing protocol

Objective:

Production of 15ml of 41%Vol hydroxyapatite slurries suitable for 3D printing.

Reagents:

Name		Acronym	Quantity	Brand
Tricalcium phosphate tribasic (Hydroxyapatite)	Ceramic	HAp	19.311 g	Macron fine chemicals
Diphenyl (2,4,6-trimethylbenzoyl) phosphine oxide	Photoinitiator	TPO	0.036g	TCI America.
Solplus D540	Dispersant	D540	1.46ml	Lubrizol Advanced Materials Inc.
Ethylene glycol dimethacrylate	Monomer	EGDMA	7.5ml	Scientific Polymer Products Inc.

Materials and equipment:

- [1] Stainless steel spatula.
- [2] Laboratory scoopula.
- [1] 1ml Luer tip syringe.
- [NA] Planetary ball mill (PBM) brand: across international.
- [10g] Agate balls (weight ratio 2:1 Hap to agate balls)
- [1] Teflon jar of 50ml for planetary ball mill with chemical resistant O-ring.
- [1] Measuring paper.
- [1] 10 ml Graduated cylinder.
- [1] Benchtop Balance.
- [NA] Parafilm film or tape.
- [10ml] Plastic syringe.
- [1] PTFE Syringe stopper.
- [NA] Aluminum foil.
- [1] Metallic tongs

Acknowledgments before beginning the procedure:

- Use protective glasses, gloves and lab coat.
- Use the fume hood for the mixing and transferring procedure.
- This procedure is to produce 15ml of Hap slurry. However, Due to the electrosteric interaction of the Hap particles with the dispersant, the resultant volume of slurry is lower.

- The planetary ball mill is in the factory campus. In the setting of this machine zero count a cycle. So, if we are working in a 50% duty cycle and it is needed to be 15min mixing. The PBM is programmed to work 2 cycles and to rest 2 cycles.

Procedure:

1. Use the weigh paper, graduated cylinder and, 1ml syringe to measure the photoinitiator TPO, the monomer of EDGMA and dispersant D540 respectively. Add all to the Teflon jar.
2. Place 10g of agate media (5 big balls and approximately 6 small balls) in the Teflon jar.
3. Set the O-ring in the cleavage of the Teflon jar. Close and seal the jar and lid with parafilm paper.
4. Install and lock the jar in the PBM. Assure that the jar is completely fastened. Mix the components for 30 minutes at 120rpm in a 50% duty cycle (3 cycles 5 min on, 5 min off).
5. Wait until step 4 finishes.
6. weigh 10g of HAp.
7. Remove the jar from the PBM and add the HAp in the solution. Mix the components with the spatula and seal the jar and lid with parafilm.
8. Fasten the jar in the PBM and set it at 300RPM for 2h in a 50% duty cycle (12 cycles of 5min on, 5min off).
9. Wait until step 8 finishes.
10. Weigh 5g of HAp.
11. Repeat step 7.
12. Fasten the jar in the PBM and set it at 320RPM for 2h in a 50% duty cycle (12 cycles of 5min on, 5min off).
13. Wait until step 11 finishes.
14. Weigh 4.311g of HAp
15. Repeat step 7.
16. Fasten the jar in the PBM and set it at 360RPM for 4h in a 50% duty cycle (12 cycles of 5min on, 5min off).

Next day to transfer the slurry to the syringes.

17. Open the jar. Collect the agate balls with the tongs and clean the walls of the jar with the spatula.
18. Mix the slurry manually for 5min.
19. Assure visually that the slurry does not show any clusters of Hap and that it is homogenous. If it is not homogenous mix manually for 5min more.
20. Transfer the slurry to the plastic syringe, close the tip of the syringe with the stopper. Wrap the syringe with aluminum foil.

APPENDIX 2: Rheology measurements procedure

Author: Katherine Lopez Ambrosio

Objective: analyze rheological behavior and viscosity of Hydroxyapatite slurries.

Materials:

1. ± 1 ml of HAp slurry per measurement.
2. Kim-wipes.
3. Stain steel spatula.
4. Ethanol.
5. Plastic pipette.
6. Gloves.
7. Rheometer with parallel plate discs of 25mm of diameter. (Located in Dr. Bailey lab).

Procedure:

- a. Set up the rheometer with the parallel plates discs and the metallic ring as shown in figure 2.a. Assure that plate discs are well attach to the machine.
- b. There are 3 bottoms on a side of the rheometer that move the mobile part up and down.
To set the gap to zero between the plates: Without sample, move the plates until the force change from negative to positive. Then, Open TA orchestrator \rightarrow control \rightarrow Gap control panel. Click on: offset torque to zero, offset force to zero and zero indicator. After, exit.
- c. Separate the plates enough to deposit the sample (fig 2.a). Carefully, Spread the sample in the plate with the spatula (fig 2.b.). Move the plates close to each other slowly and try to set the gap to the predetermine value set for the experiment (For this case near to 1.1 mm). If you do not have a predetermine gap value, choose one having in account that it should be at least 3 times bigger than the size of your particles, and so forth continue using the same value to compare data accurately.

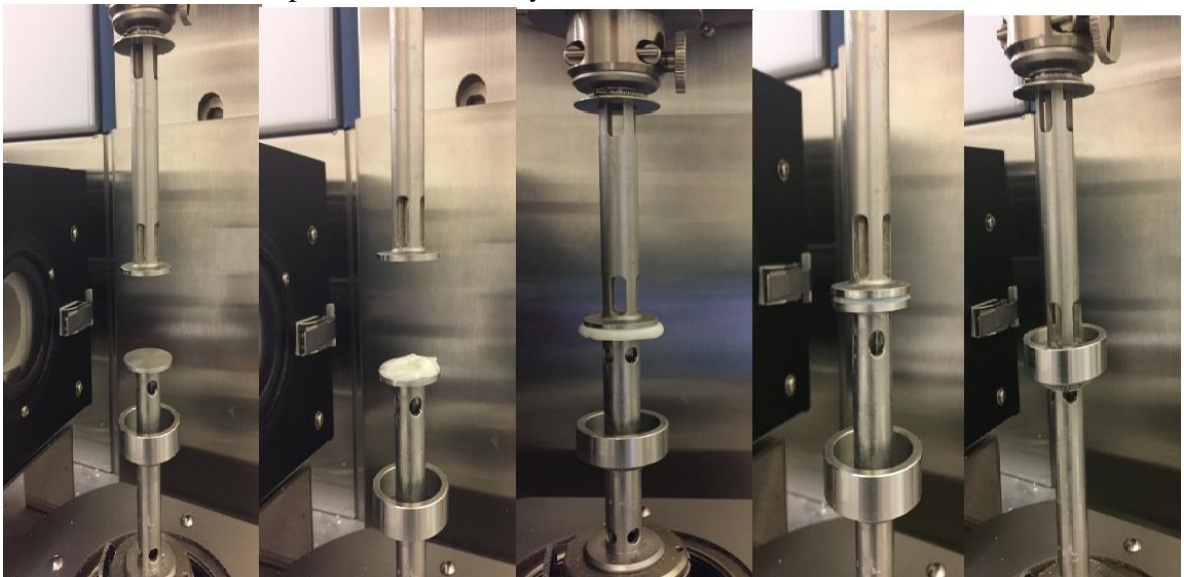


Figure 2.a.b.c.d.e.

- d. Clean the excess of material from the plates(fig2c.d.). Pull the metallic ring up (fig2.e).
- e. Go to TA orchestrator, control→ edit/start test. Type title (name of the sample), folder (James group/katherine), choose geometry: in this case parallel plate, test set up: predefined test setups, strain-controlled, transient, step rate test (fig3.). Then, go to edit test: sampling mode Linear, points per zone 20, shear rate:0.1, 1, 10 and 100 S⁻¹, zone time 20s each zone, options delay on (fig4.).

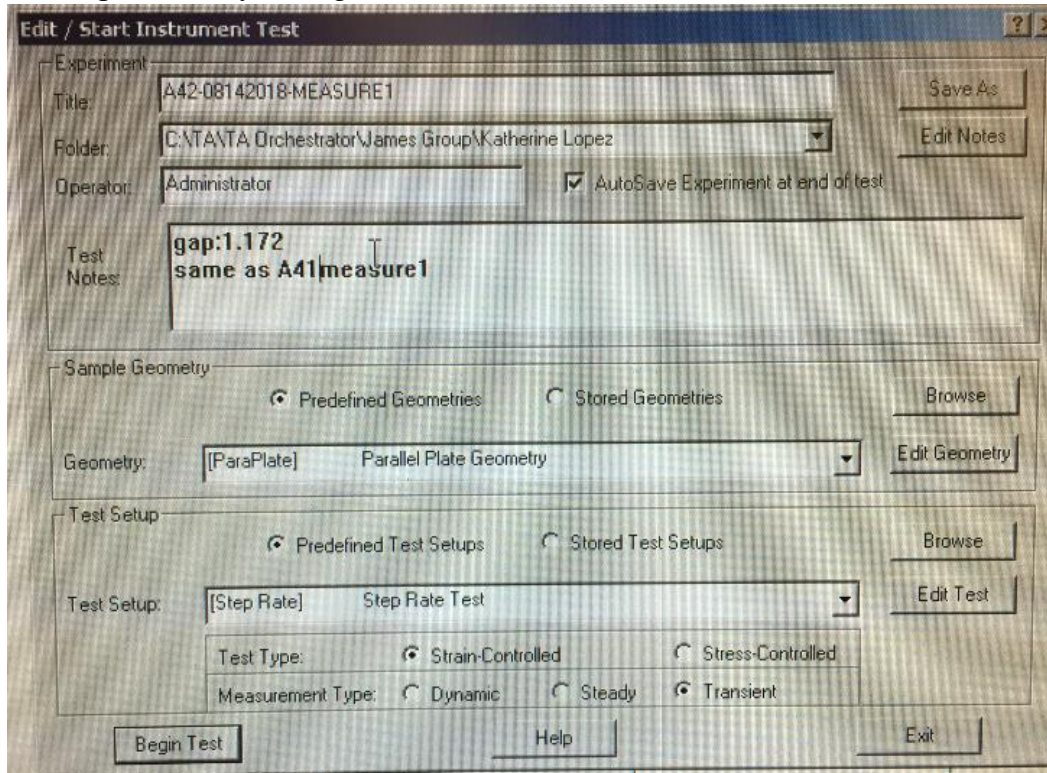


Figure3.

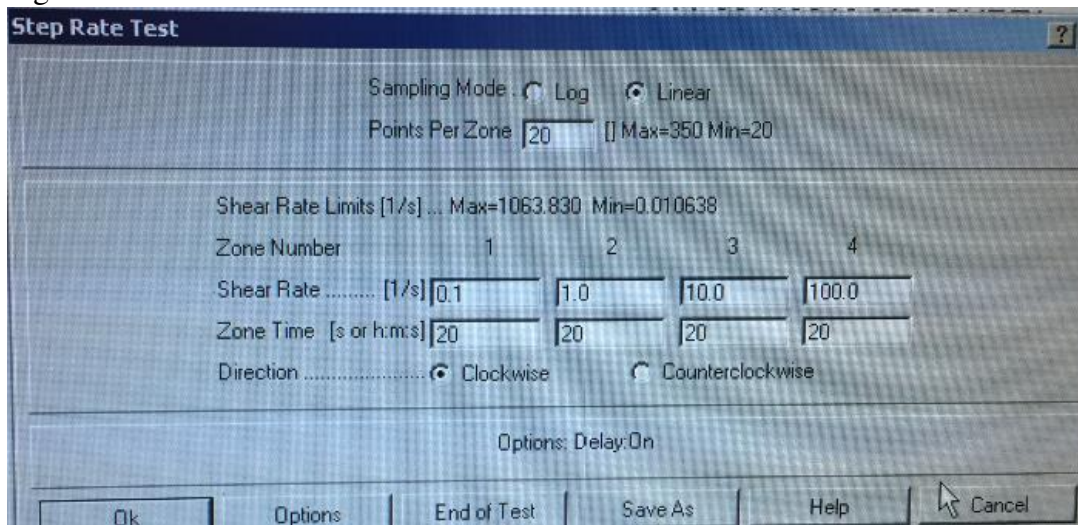


Figure4.

- f. From the moment you set the gap with the sample in, wait 5min to begin the test. This is necessary, so the sample can relax after the stress that was applied with the spatula and the top disc.
- g. Let the experiment run. When it finishes, clean the sample and clean the ring and the parallel plates with ethanol. Assure that they are completely clean before adding the next sample.
- h. If another measurement is going to be made, repeat c through f steps. If you are done, unattach the parallel plates from the machine, clean everything, save it the accessories in the black box and register yourself in the folder.

APPENDIX 3. Protocol to polish HAp/PEGDMA samples

Author: Katherine Lopez Ambrosio

Objective:

Eliminate surface defects and level surface of printed samples.

Materials:

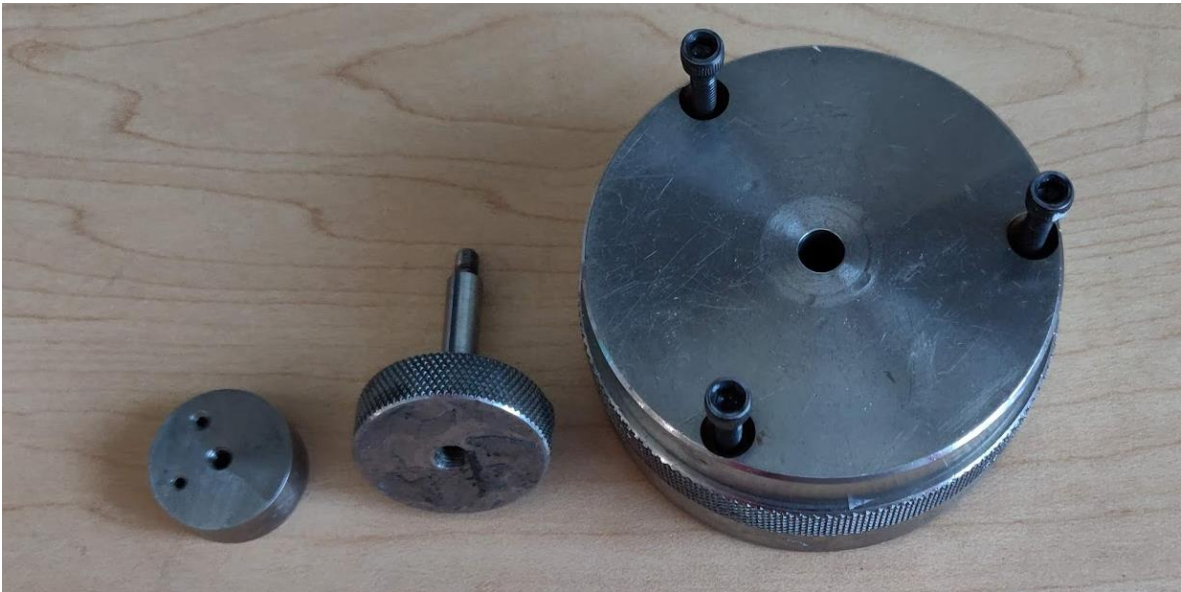
- Sample
- Grinding paper (grits to use depend on the level of finishing desired to obtain)
- Super glue
- Tape
- Acetone
- Gloves
- Tweezers
- Razor blade
- Ethanol
- Hand polishing fixture. (Dr. Ma lab), (photo1,2,3)
- Metallic disc that attaches to the hand polishing fixture (Dr. Ma lab)

Advice before you begin:

1. A lot of samples break in the polishing process so have additional number of samples than required.
2. Samples are very brittle so all the movements to polish the samples must be done softly.
3. Hand polishing fixture needs to be used to obtain even surfaces. If samples are polishing with bare hands the force applied by the thumb finger is going to be different than the force applied by the index finger leading to uneven surface.

Procedure:

1. Stick tape in the metal of the length of your sample.
2. Put super glue in the sample and attach it to the top of the tape that is in the metallic fixture. Press the sample against the fixture.
3. Let the sample dry completely.
4. Begin with lower grit number 800. Make movements in just one direction in different parts of the sandpaper.
5. Stop when you cannot see defects
6. Clean sample surface and hand fixture with ethanol
7. Polish the sample with a higher grit number 1000 or 1200 with one movement direction.
8. Clean the surface with ethanol
9. Acetone will dissolve the tape and help to detach the sample with soft movements.





APPENDIX 4: Power density of 405nm light source Hyrel 3D printer

These measurements were taken from a distance of the light source of 38mm.

